

# UCSF

## UC San Francisco Previously Published Works

### Title

Rotor Localization and Phase Mapping of Cardiac Excitation Waves Using Deep Neural Networks.

### Permalink

<https://escholarship.org/uc/item/8j64t88p>

### Authors

Lebert, Jan

Ravi, Namita

Fenton, Flavio

et al.

### Publication Date

2021

### DOI

10.3389/fphys.2021.782176

Peer reviewed



# Rotor Localization and Phase Mapping of Cardiac Excitation Waves Using Deep Neural Networks

Jan Lebert<sup>1</sup>, Namita Ravi<sup>1,2</sup>, Flavio H. Fenton<sup>3</sup> and Jan Christoph<sup>1\*</sup>

<sup>1</sup> Cardiovascular Research Institute, University of California, San Francisco, San Francisco, CA, United States, <sup>2</sup> Yale School of Medicine, Yale University, New Haven, CT, United States, <sup>3</sup> School of Physics, Georgia Institute of Technology, Atlanta, GA, United States

## OPEN ACCESS

### Edited by:

Elena Tolkacheva,  
University of Minnesota Twin Cities,  
United States

### Reviewed by:

Caroline Helen Roney,  
King's College London,  
United Kingdom  
Maria S. Guillem,  
Universitat Politècnica de València,  
Spain

### \*Correspondence:

Jan Christoph  
jan.christoph@ucsf.edu

### Specialty section:

This article was submitted to  
Cardiac Electrophysiology,  
a section of the journal  
Frontiers in Physiology

**Received:** 23 September 2021

**Accepted:** 11 November 2021

**Published:** 17 December 2021

### Citation:

Lebert J, Ravi N, Fenton FH and  
Christoph J (2021) Rotor Localization  
and Phase Mapping of Cardiac  
Excitation Waves Using Deep Neural  
Networks. *Front. Physiol.* 12:782176.  
doi: 10.3389/fphys.2021.782176

The analysis of electrical impulse phenomena in cardiac muscle tissue is important for the diagnosis of heart rhythm disorders and other cardiac pathophysiology. Cardiac mapping techniques acquire local temporal measurements and combine them to visualize the spread of electrophysiological wave phenomena across the heart surface. However, low spatial resolution, sparse measurement locations, noise and other artifacts make it challenging to accurately visualize spatio-temporal activity. For instance, electro-anatomical catheter mapping is severely limited by the sparsity of the measurements, and optical mapping is prone to noise and motion artifacts. In the past, several approaches have been proposed to create more reliable maps from noisy or sparse mapping data. Here, we demonstrate that deep learning can be used to compute phase maps and detect phase singularities in optical mapping videos of ventricular fibrillation, as well as in very noisy, low-resolution and extremely sparse simulated data of reentrant wave chaos mimicking catheter mapping data. The self-supervised deep learning approach is fundamentally different from classical phase mapping techniques. Rather than encoding a phase signal from time-series data, a deep neural network instead learns to directly associate phase maps and the positions of phase singularities with short spatio-temporal sequences of electrical data. We tested several neural network architectures, based on a convolutional neural network (CNN) with an encoding and decoding structure, to predict phase maps or rotor core positions either directly or indirectly via the prediction of phase maps and a subsequent classical calculation of phase singularities. Predictions can be performed across different data, with models being trained on one species and then successfully applied to another, or being trained solely on simulated data and then applied to experimental data. Neural networks provide a promising alternative to conventional phase mapping and rotor core localization methods. Future uses may include the analysis of optical mapping studies in basic cardiovascular research, as well as the mapping of atrial fibrillation in the clinical setting.

**Keywords:** atrial fibrillation, cardiac electrophysiology, spiral waves, phase singularity, catheter mapping, optical mapping, neural networks, artificial intelligence

## 1. INTRODUCTION

Cardiac muscle cells constantly oscillate between an “excited” and a “resting” electrical state, allowing us to assign a phase  $\phi$  to the state of each cell during this cycle. Cardiac mapping techniques, such as catheter electrode mapping or voltage-sensitive optical mapping, measure the spread of electrical impulses across the heart surface and visualize the spatio-temporal evolution of electrical activity. These visualizations are frequently depicted as phase maps  $\phi(\vec{x}, t)$ , which uniquely represent the time course of the action potential in each location of the tissue and express the synchronicity of the activation in both space and time. Phase maps are particularly suited to characterize the spatio-temporal disorganization of the electrical wave dynamics underlying cardiac fibrillation (Winfree, 1989; Gray et al., 1998; Witkowski et al., 1998; Nash et al., 2006; Umapathy et al., 2010; Christoph et al., 2018). During fibrillation, the heart’s electrophysiology degenerates into a dynamic state driven by chaotic wave phenomena, which propagate rapidly through the heart muscle and cause irregular, asynchronous contractions. These inherently three-dimensional wave phenomena can be observed on the heart’s surface using optical mapping, where they often take the shape of rapidly rotating spiral vortex waves or “rotors”. Phase maps depict these rotors as pinwheel patterns, with each pinwheel consisting of lines of equal phase that merge at the rotational center of the vortex wave. The topological defect at the vortex’s core is referred to as a phase singularity. During ventricular fibrillation, phase singularities move across the heart surface, interact with each other, and undergo pairwise creation and annihilation. Phase singularities provide a means to automatically localize and track reentrant vortex waves through the heart muscle. They can be used to track wavebreaks (Liu et al., 2003; Zaitsev et al., 2003), or interactions of vortex cores with the underlying substrate (Valderrabano et al., 2003), to simplify the visualization of three-dimensional scroll wave dynamics (Fenton and Karma, 1998; Clayton et al., 2006), and to measure fluctuations in the complexity of the dynamics (Zaritski et al., 2004). In short, phase singularities are an elegant way to characterize high-frequency arrhythmias that involve reentrant vortex waves, such as ventricular fibrillation (VF) or atrial fibrillation (AF) (Nattel et al., 2017).

Various methods have been proposed to compute phase maps and phase singularities (PS). These methods have been applied to both simulations of VF (Fenton and Karma, 1998; Bray et al., 2001; Clayton et al., 2006) and AF (Hwang et al., 2016; Rodrigo et al., 2017), as well as experimental data, including electrode recordings of human VF (Nash et al., 2006; Umapathy et al., 2010) and human AF (Kuklik et al., 2015; Podziemski et al., 2018; Abad et al., 2021) optical maps of the transmembrane potential during VF (Gray et al., 1998; Iyer and Gray, 2001; Bray and Wikswo, 2002; Rogers, 2004; Christoph et al., 2018) and AF (Yamazaki et al., 2012; Guillem et al., 2016) in isolated hearts, optical maps of action potential spiral waves in cardiac cell cultures (Bursac et al., 2004; Entcheva and Bien, 2006; Munoz et al., 2007; Umapathy et al., 2010; You et al., 2017), and time-varying 3D maps of mechanical strain waves measured

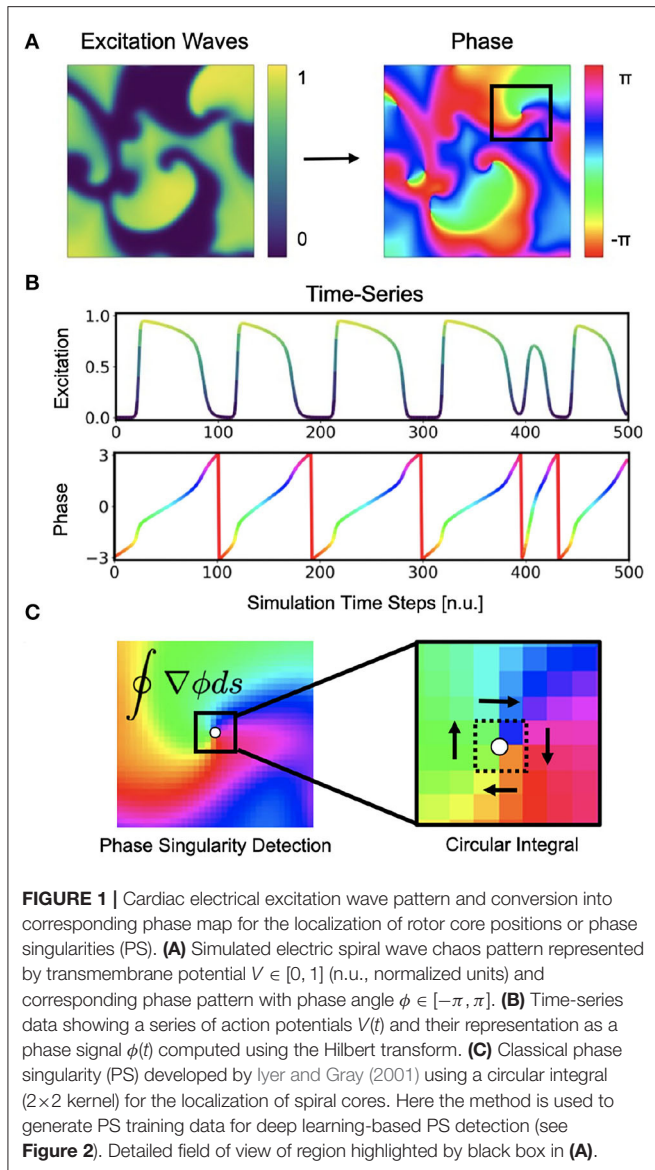
during VF in isolated hearts using ultrasound (Christoph et al., 2018). However, phase maps and PS are prone to measurement artifacts and deficits caused by inadequate processing of the measurement data, particularly when the data is noisy or sparse (King et al., 2017; Kuklik et al., 2017; Rodrigo et al., 2017; Roney et al., 2017, 2019; You et al., 2017). Noise and motion artifacts are a frequent issue when analyzing optical mapping recordings (Zou et al., 2002; Christoph and Luther, 2018). Electrode mapping, used in both basic research and the clinical setting, is limited by low spatial resolution, or sparsity, even with the use of multi-electrode arrays and 64-lead basket catheters.

Mapping fibrillatory wave phenomena at low resolutions can lead to misrepresentation of the underlying dynamics. For example, low resolution phase mapping has been shown to create false positive detections of PS (King et al., 2017; Kuklik et al., 2017; Roney et al., 2017, 2019; You et al., 2017), contributing to much uncertainty in the imaging-based diagnosis of AF, a field in which rotors remain a highly controversial concept (Aronis et al., 2017; Nattel et al., 2017; Schotten et al., 2020). Mapping of AF would greatly benefit from computational methods, which could account for low spatial resolution and produce reliable visualizations of electrical phenomena from sparse and noisy spatio-temporal electrical signals.

In this study, we demonstrate that deep convolutional neural networks (CNNs) can be used to compute phase maps and phase singularities from short spatio-temporal sequences of electrical excitation wave patterns, even if these patterns are very sparse and very noisy. We use variations of two-stage encoder-decoder CNNs with an encoding stage, a latent space, and a decoding stage (see **Figure 2**). The neural network associates electrical excitation wave patterns with phase maps and phase singularity (PS) positions during a training procedure. After training, it is subsequently able to translate electrical excitation wave patterns into phase maps and PS when applied to new, previously unseen data. We tested two versions of the neural network with an integrated convolutional long short-term memory (LSTM) module in the latent space of the original encoder-decoder architecture and a U-Net architecture with skip-connections. Regardless of the particular architecture, the network was able to predict phase maps and PS in both experimental and synthetic data robustly and with high accuracy. When presented with sparse electrical data from a short temporal sequence of only 1–5 snapshots of electrical activity, the network maintained a robust accuracy level, even in the presence of strong noise. The approach may supersede more classical approaches due to its efficiency, its robustness against noise, and its ability to inter- and extrapolate missing measurement data with only minimal spatial and temporal information.

### 1.1. Phase Mapping and Phase Singularity Detection Techniques

Phase maps and phase singularities (PS) have been used to characterize cardiac fibrillation for over 30 years (Winfree, 1989), and various methods were introduced to compute PS either directly or indirectly (see **Figure 1C**). In computer simulations,



the computation of a phase state or PS is straight-forward as the dynamic variables from the equations describing the local electrical state are readily available in the simulation and can be used to define a phase angle instantaneously (Krinsky et al., 1992). For instance, with  $V$  and  $r$  for electrical excitation and refraction, respectively, see Equations (4)–(5), the phase angle can be defined as  $\phi = \arctan2(V, r)$  (see also **Figure 3A**). Likewise, level-set methods using isocontour lines of two dynamic variables, such as  $V$  and  $r$ , can be used to locate PS directly as the intersection points of these isocontours (Barkley et al., 1990). However, with experimental data, there is typically only one measured variable, such as the transmembrane voltage or an electrogram, and it is accordingly not possible to define a phase without additional temporal information. With experimental data, it becomes necessary to construct a phase signal  $\phi(t)$  from a single measured time-series  $V(t)$  using

techniques such as (i) delay embedding (Gray et al., 1998):

$$\phi(t) = \arctan2(V(t), V(t + \tau)) \quad (1)$$

with an embedding delay  $\tau$ , typically defined as  $\sim 1/4$  of the average cycle length or the first zero-crossing of the auto-correlation function, or (ii) the Hilbert transform  $\mathcal{H}(t)$ , which generates the complex analytical signal of a periodic signal from which in turn the phase

$$\phi(t) = \text{Re}(\mathcal{H}(t)) \quad (2)$$

can be derived (Bray and Wikswo, 2002). The most intuitive approach to compute a time-dependent phase signal  $\phi(t)$  of a sequence of action potentials is to detect the upstrokes of two subsequent action potentials and to define a piecewise linear continuous function  $\phi_L(t)$ , which linearly interpolates the phase angle from  $-\pi$  to  $\pi$  between the two upstrokes. The Hilbert transform generates a phase signal  $\phi_{\mathcal{H}}(t)$  which is very similar to the linearly interpolated phase signal  $\phi_L(t)$  (see **Figure 1B**).

Phase singularities can then be calculated (see **Figure 1C**), by using the circular line integral method developed by Iyer and Gray (2001) summing the gradient of the phase along a closed circular path  $s$  around a point  $\vec{x} = (x, y)$  in the phase plane:

$$\oint \nabla \phi(x, y; t) ds = \pm 2\pi \quad (3)$$

If the circular path is sufficiently small (typically around  $2 \times 2$  pixels), the integral yields  $\pm 2\pi$  when the line integral encloses a phase singularity (the sign indicates chirality), or 0 if it does not enclose a phase singularity. As the line integral method calculates the spatial gradient of the phase, it is very sensitive to noise and requires continuous and smooth phase maps. Therefore, much prior work has focused on improving the robustness of phase mapping and PS detection methods under more realistic conditions, e.g. with noise or other artifacts that typically occur with, for instance, contact electrode measurements. Zou et al. (2002) further refined the line integral method using convolutions and image analysis. Kuklik et al. (2015) introduced sinusoidal recomposition to remove undesired high-frequency components during the computation of phase signals using the Hilbert transform. In contrast to the line integration method, Tomii et al. (2016) proposed computing the phase variance to locate PS. Similarly, Lee et al. (2016) introduced a so-called “location-centric” method to locate PS, the method only requiring temporal information about the voltage at the core. Li et al. (2018) introduced a Jacobian-determinant method using delay embedding for identifying PS also without explicitly computing a phase. Marcotte and Grigoriev (2017) and Gurevich et al. introduced level-set methods to compute PS in noisy conditions and demonstrated the robustness of the approach with VF optical mapping data (Gurevich et al., 2017; Gurevich and Grigoriev, 2019). Vandersickel et al. (2019) proposed to use graph theory to detect rotors and focal patterns from arbitrarily positioned measurement sites. Mulimani et al. (2020) used CNNs to detect the core regions of simulated spiral waves using a CNN-based classification approach and discriminating

sub-regions containing spiral wave tips from areas exhibiting other dynamics, and consequently generated low-resolution heat maps indicating the likely and approximate core regions of spiral waves. Very similarly, Alhusseini et al. (2020) used CNNs to classify and discriminate rotational and non-rotational tiles in maps of AF acquired with basket catheter electrode mapping. Lastly, Li et al. (2020) provided a comparison of 4 different PS detection algorithms applied to AF and found that results can vary significantly.

## 2. METHODS

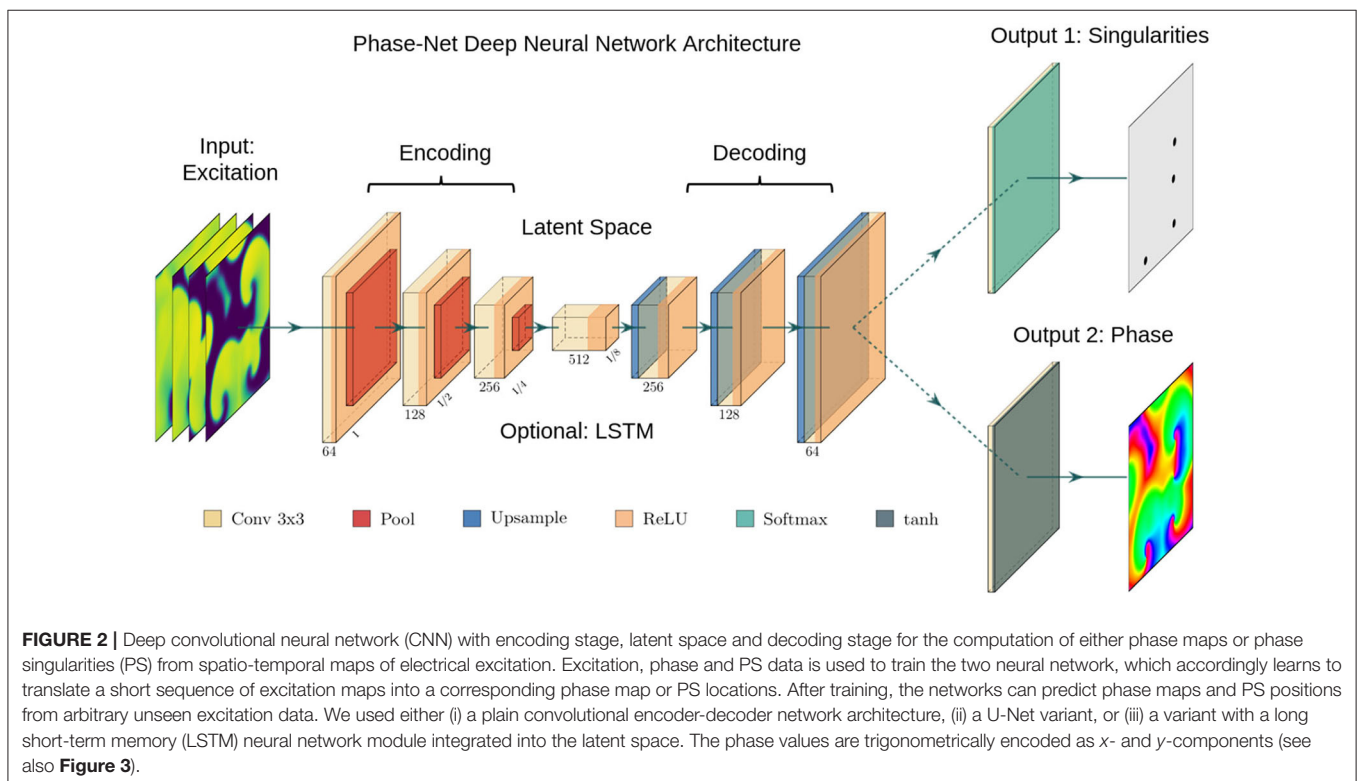
We developed a two-stage deep convolutional neural network (CNN) with encoder and decoder architecture and trained the network with pairs of two-dimensional maps showing electrical excitation wave patterns and corresponding “ground truth” phase maps and phase singularity (PS) locations. The training was performed with both simulation data and experimental data, which was obtained in voltage-sensitive optical mapping experiments in two different species during ventricular fibrillation (VF). After training, the network was applied to new data and used to predict phase maps or the positions of PS from “unseen” excitation wave patterns.

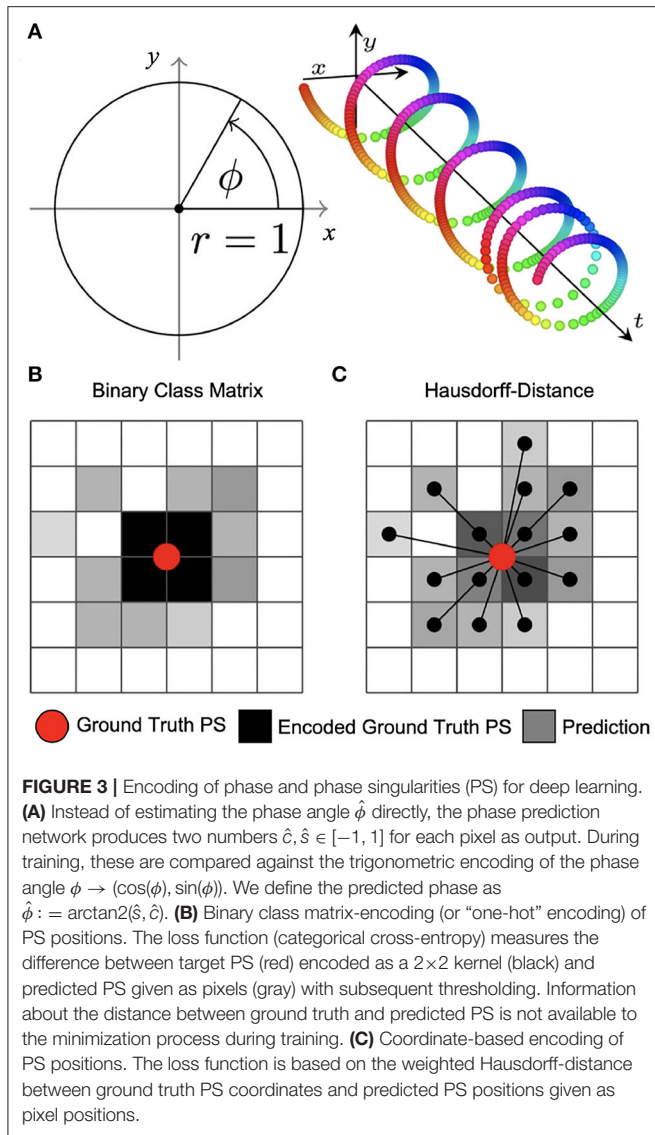
### 2.1. Neural Network Architecture

The architecture of our neural networks comprises an encoding stage, a latent space, and a decoding stage (see **Figure 2**). The neural networks are designed to translate an arbitrary two-dimensional electrical excitation wave pattern or a short

sequence of two-dimensional excitation wave patterns into either a corresponding two-dimensional phase map, or predict the positions of phase singular points (PS) in the electrical maps. We developed three phase map prediction neural network models M1, M2, and M3, and two different PS prediction neural network models M1A and M1B which are based on M1. The three phase map prediction models are a basic encoder-decoder CNN version M1, an LSTM-version M2 and a U-Net version M3, see below for details. The difference between models M1A and M1B is mainly the associated loss function and the encoding of the ground truth PS. M1A uses a pixel-wise cross-entropy loss which does not account for the distance between predicted PS locations and ground truth PS locations unless they overlap, whereas M1B uses a loss function based on the distance between predicted and ground truth PS locations.

The phase map prediction neural networks are trained with excitation wave patterns as input and a two-dimensional trigonometric encoding of the phase map as target (see **Figure 3A**). The trigonometric encoding eliminates the discontinuity of a linear encoding of the cyclic phase  $\phi$  by encoding the value onto a two-dimensional unit circle:  $\phi \rightarrow (\cos(\phi), \sin(\phi)) =:(c, s)$ . Therefore, the two phase mapping CNNs have a two-dimensional layer with two channels as output, which are estimates of the sine  $\hat{s}$  and cosine  $\hat{c}$  of the phase angle  $\phi$ . The predicted phase  $\hat{\phi}$  is decoded as  $\hat{\phi} := \arctan2(\hat{s}, \hat{c})$ . We use the hyperbolic tangent function as activation function in the last layer of the phase mapping CNNs to ensure that  $\hat{c}, \hat{s} \in [-1, 1]$ . All models are based on a convolutional encoder-decoder architecture (see **Figure 2**). However, whereas model





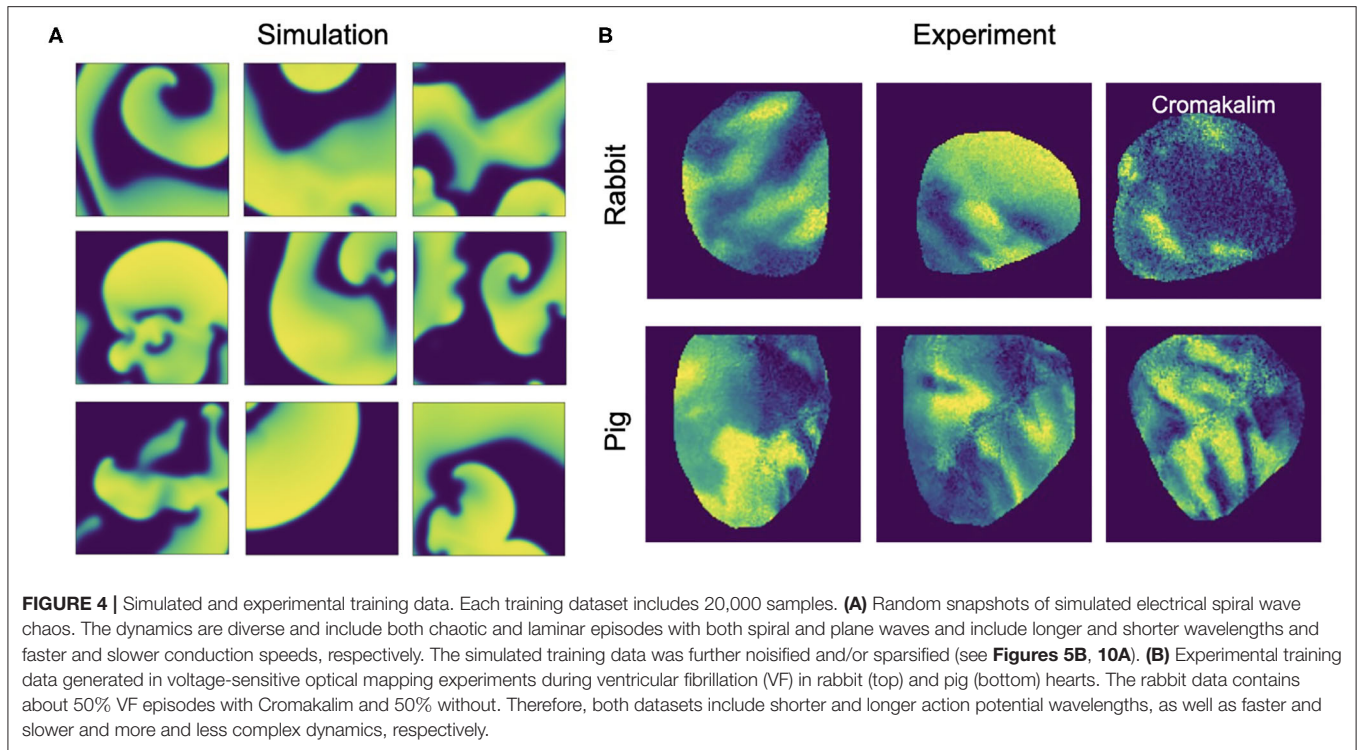
M1 uses a two-dimensional convolutional layer in the latent space, the latent space of model M2 is a two-dimensional convolutional long short-term memory (LSTM) neural network layer (Hochreiter and Schmidhuber, 1997; Shi et al., 2015), and model M3 is based on the generic convolutional architecture of model M1, but includes long skip connections at each maxpooling/upsampling step, similar to U-Net (Ronneberger et al., 2015). In all models the encoder- and decoder-stage consist of three two-dimensional convolutional layers, each followed by a batch normalization layer (Ioffe and Szegedy, 2015), rectified linear unit (ReLU) activation layer (Nair and Hinton, 2010), and a maxpooling or upsampling layer. The convolutional layers use 64, 128, and 256 kernels in the encoding stage, 512 kernels in the latent space, and 256, 128, and 64 kernels in the decoder stage. The phase prediction models use the mean squared error as loss function.

The two PS prediction neural networks M1A and M1B are trained with excitation wave patterns as input and either (i) a dense binary class matrix representation of PS positions or (ii) coordinates of PS positions as target, respectively (see Figures 3B,C). The ground truth PS are located—by construction (see Figure 1C)—in the center of a  $2 \times 2$  kernel. With model M1A we set 1 as target for all four neighboring pixels of a PS and 0 for all other pixels. While it is possible to train directly on such an encoding with a binary cross-entropy loss function, we achieved better accuracies when using a categorical encoding of the target image as a  $128 \times 128 \times 2$  class matrix, where in the first channel all non-PS pixels are valued 1 and in the second channel all  $2 \times 2$  PS pixels are 1 and 0 otherwise. Accordingly, model M1A uses two output layers with a softmax activation function, and categorical cross-entropy as a loss function during training. Note that the loss corresponds to a pixel-wise loss, which does not take into account distances between ground-truth and approximated PS positions. With model M1B the target PS are encoded directly as a list of two-dimensional  $(x, y)$ -coordinates of PS positions and the loss function uses a weighted Hausdorff-distance with the parameter  $\alpha = -3$  between the target PS and predicted pixel distributions approximating PS positions, which was introduced by Ribera et al. (2019) for the deep learning-based localization of objects (see illustration in Figure 3C). Note that the loss function includes information about spatial distances between ground-truth and approximated PS during training. Model M1B comprises one output layer with a sigmoid activation function and we used a threshold of 0.5 to obtain a binary PS prediction image. For both models M1A and M1B the predicted PS positions are computed as sub-pixel precise PS locations from the center of each connected object in the binary PS prediction image. Two pixels are connected (belong to the same object), if both are 1 and when their edges or corners are adjacent.

All network models analyze either a single, static two-dimensional excitation wave pattern or a short sequence of up to 10 excitation wave patterns as input. The patterns consist of consecutive snapshots of the activity sampled at the current time step  $t$  and at equidistant time intervals at previous time steps, see also section 2.2. Note that, if we refer to “video images / frames / excitation patterns” or “samples,” each of these samples may refer to a single or a short series of 2 – 10 two-dimensional excitation patterns. For model M1 and M3 the excitation wave patterns are represented as input channels, while for model M2 each temporal excitation wave pattern is processed separately in the neural network as the LSTM is a recurrent neural network. All neural network models were implemented in Tensorflow (Abadi et al., 2015) version 2.6.0.

## 2.2. Training Data Generation

We generated synthetic training data using a phenomenological computer model of cardiac electrophysiology (Aliev and Panfilov, 1996). In short, non-linear waves of electrical excitation and refractoriness were modeled using partial differential equations and an Euler finite differences numerical



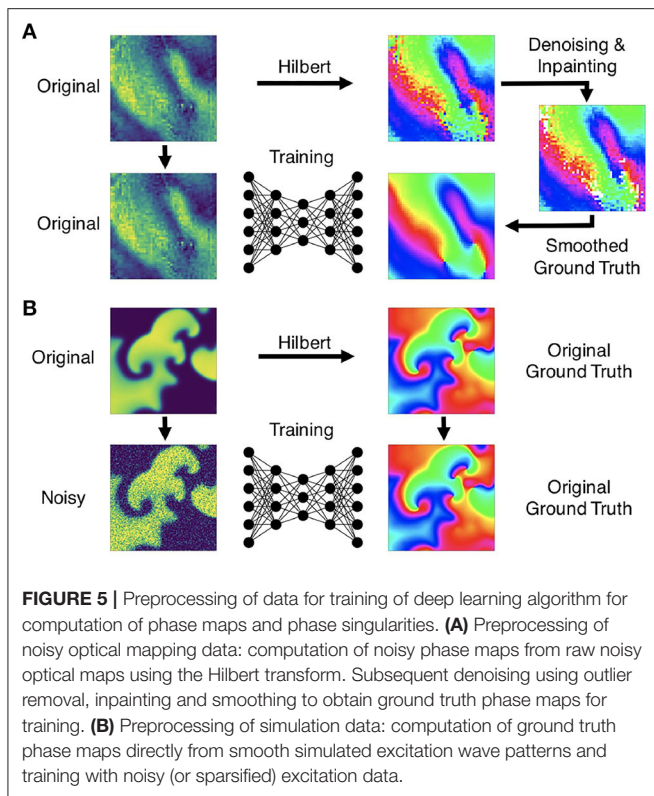
integration scheme:

$$\frac{\partial V}{\partial t} = \nabla^2 V - kV(V - a)(V - 1) - Vr \quad (4)$$

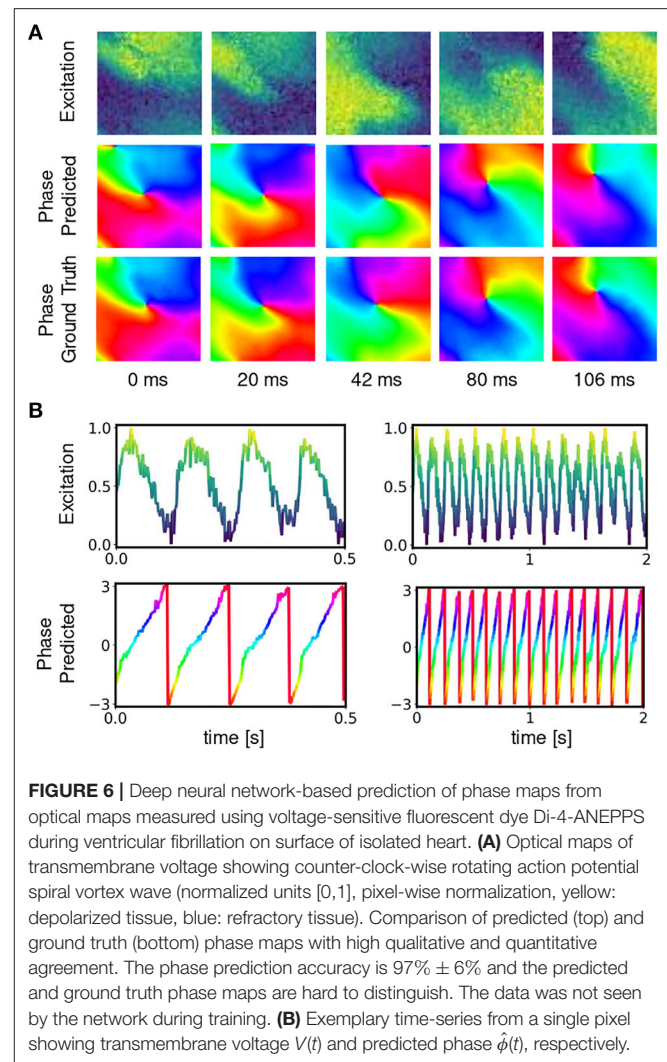
$$\frac{\partial r}{\partial t} = \epsilon(V, r)(kV(a + 1 - V) - r) \quad (5)$$

Here,  $V$  and  $r$  are dimensionless, normalized dynamic variables for electrical excitation (voltage) and refractoriness, respectively. Together with the isotropic diffusive term  $\nabla^2 V = \nabla \cdot (D\nabla V)$  with the diffusion constant  $D = 1.0$  in Equation (4), the model produces non-linear waves of electrical excitation and the term  $\epsilon(V, r) = \epsilon_0 + \mu_1 r / (V + \mu_2)$  in Equation (5) and electrical parameters  $k$ ,  $a$ ,  $\epsilon_0$ ,  $\mu_1$ , and  $\mu_2$  influence properties of the excitation waves. The size of the two-dimensional simulation domain was  $200 \times 200$  cells/pixels. The parameters were set to  $a = 0.09$ ,  $k = 8.2$ ,  $\epsilon_0 = 0.01$ ,  $\mu_1 = 0.07$ ,  $\mu_2 = 0.3$  and spiral wave chaos was initiated by applying a series of point stimulations in random locations. With the chosen parameters the dynamics exhibit both chaotic spiral wave and more laminar wave dynamics with strong fluctuations in the complexity of the wave patterns (see **Figures 4A, 9F** and **Supplementary Videos 2, 4**). We generated 20 episodes with a series of 2,500 snapshots of the dynamics in each episode. **Figure 1A** shows an example of such a snapshot. The 2,500 snapshots show about 25 spiral wave rotations. Correspondingly, one spiral rotation is resolved by about 100 snapshots. Note that in the simulation the dynamics are resolved at a  $10 \times$  higher temporal resolution than in the series of snapshots, because we stored a snapshot only in every 10th simulation time step. In total, we obtained 50,000 snapshots, from which we then created

20,000 training samples (see **Figure 4A**), where one training sample comprises a short sequence of snapshots with up to 10 images of the excitation. Within the sequence, the first snapshot, denoted with  $t_0$ , corresponds to the snapshot at time  $t$  in the video. The training is performed with the corresponding ground truth phase maps and PS obtained at this time step  $t$  and, correspondingly, the network also predicts a phase map or PS at time  $t$ . The other snapshots in each sample correspond to snapshots showing the dynamics at previous time steps  $t_{-1}$ ,  $t_{-2}$  etc., where  $t_{-i} = t_0 - i \cdot \tau$  with  $i = 1, \dots, N_t$  and  $N_t$  is the number of snapshots in the sample and  $\tau$  is the temporal sampling distance between the frames over parts of the previous period. The parameters  $N_t$  and  $\tau$  are discussed in more detail in section 3.5 and in **Figure 13**. The training samples were shuffled in time, while the temporal sequence within each sample was kept in its original order. We generated test data for evaluation that was not used during training by simulating 5,000 snapshots separately using the same electrical parameters and generating samples with the same parameters  $N_t$  and  $\tau$  for testing purposes. We computed ground truth phase maps from the original series of excitation snapshots before shuffling using the Hilbert transform (Bray and Wikswo, 2002) and computed ground truth PS using the Iyer and Gray (2001) line integral method, as shown in **Figures 1B,C**. To simulate noisy excitation wave data, we added noise to the training data (see **Figure 5**). The Gaussian white noise was added to the individual pixels independently in each frame and independently over time ( $\sigma = 0.1, 0.2, \dots, 0.8$  states the standard deviation of the noise). Each excitation snapshot was optionally additionally sparsified by setting masked excitation values to 0.



We generated experimental training data using high-speed video data obtained in optical mapping experiments with voltage-sensitive fluorescent dyes (Di-4-ANEPPS). Imaging was performed during VF in isolated rabbit ( $N = 2$ ) and porcine ( $N = 5$ ) hearts at acquisition speeds of 500 fps, respectively, using a Teledyne Photometrics Evolve camera ( $128 \times 128$  pixels). The rabbit data included 6 recordings with 4 different views and more than 25,000 video frames in total. The pig data included 10 recordings with 8 different views and more than 100,000 video frames in total. About half of the rabbit data shows VF episodes with the potassium channel opener Cromakalim, which typically reduces the action potential duration and accelerates VF dynamics. The raw optical mapping videos were pixel-wise normalized in time using a sliding-window normalization (window size 100–120 frames). We used the Hilbert transform to compute phase maps of the pixel-wise normalized optical maps, the phase maps were subsequently denoised and smoothed, see **Figure 5A** and section 2.5, to obtain ground truth phase maps. These ground truth phase maps were then used to compute ground truth PS using the circular integral method as with the simulation data. 20,000 samples of the pixel-wise normalized noisy versions of the voltage-sensitive optical maps (without spatio-temporal smoothing), ground truth phase maps, and PS were used as training dataset for each species. The test datasets consisted of 5,000 samples, which were derived from 1–2 separate recordings, which were left out of the training dataset. Each training or test sample corresponds to a short series (10 frames) of voltage-sensitive optical maps showing action potential wave

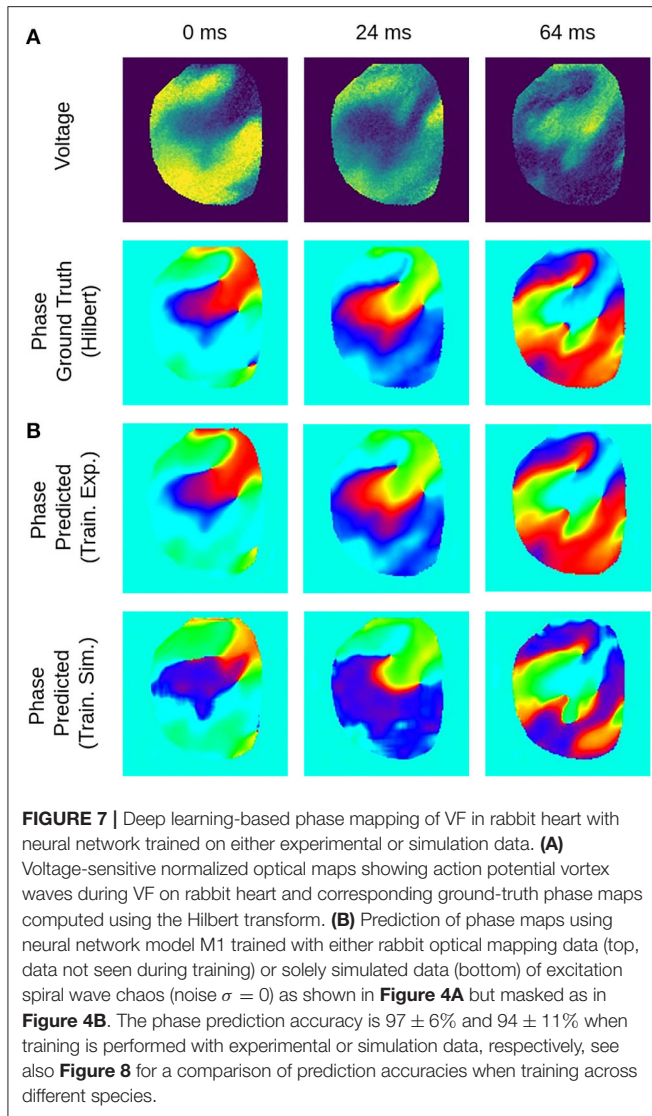


dynamics in analogy to the simulation data. The experimental samples were masked with masks outlining the shape of the heart. Pixels outside of the mask were set to 0. The same masks were also applied to simulated data (see **Supplementary Video 2**).

### 2.3. Training Procedure

Using the experimental and simulated data described in section 2.2, we generated training datasets consisting of corresponding two-dimensional electrical excitation wave data and phase maps as well as  $(x, y)$  positions of PS in these maps. The simulated data was resized from  $200 \times 200$  pixels to  $128 \times 128$  pixels to match the size of the experimental data. All predictions were performed on a separate dataset, which was not part of the training. The predictions in **Figures 6–15** were only performed on “unseen” data, which the neural network was not exposed to during training. A fraction of 5% of the samples of the training datasets were used for validation during training. The networks were trained with a batch size of 32 using the Adam (Kingma and Ba, 2015) optimizer with a learning rate of 0.001. All models were typically trained for 10 to 15





epochs on data including 20,000 frames or samples, if not stated otherwise.

## 2.4. Phase Mapping and Rotor Localization Accuracy

The phase prediction accuracy was determined by calculating the angular accuracy,  $1 - \langle |\Delta\phi| \rangle / \pi$ , where  $|\Delta\phi|$  is the minimum absolute angle difference between the predicted phase  $\hat{\phi}_i(x, y)$  and the ground truth phase  $\phi_i(x, y)$ . The average absolute angle difference

$$\langle |\Delta\phi| \rangle = \frac{1}{N \cdot N_{\text{pixels}}} \sum_{i,x,y} |\Delta\phi_i(x, y)| \quad (6)$$

is evaluated over all  $N_{\text{pixels}}$  pixels  $(x, y)$  in all  $N$  test samples  $i$ . All uncertainties of the phase prediction accuracies stated throughout this study correspond to the standard deviation of the angular accuracy over all  $N_{\text{pixels}}$  pixels in all  $N$  samples

in the entire testing dataset. The PS prediction accuracy was evaluated with the precision, recall, and F-score based on the number of true positive  $tp$ , false positive  $fp$  and false negative  $fn$  PS predictions, as well as the mean absolute error of the number of predicted PS and the mean average Hausdorff distance. A true positive estimated PS position is counted if any estimated PS location is within at most  $r$  pixels from the ground truth PS. A false positive is counted if no ground truth PS is located within a distance of  $r$  from the estimated PS position. A false negative is counted if a ground truth PS does not have any estimated PS within a distance of at most  $r$ . We chose  $r = 3$  pixels, see also **Figure 9E**. We note that this definition is biased in favor of the prediction when two PS are predicted within  $r$  pixels of a single ground truth PS, as both predicted PS will be counted as true positive. However, by construction of the prediction method (see **Figure 3** and section 2.1) this case occurs only very rarely. E.g., for none of the models presented in **Table 1** did this situation occur for more than 15 PS out of a total of  $\sim 17,000$  predicted PS. The bias in favor of the model is thus negligible for the precision, recall and F-score. Precision is  $tp/(tp + fp)$ , the proportion of estimated PS locations that are close enough to a ground truth PS location. Recall is  $tp/(tp + fn)$ , the proportion of the true phase singularities the neural network is able to detect. The F-score is the harmonic mean of precision and recall:

$$\text{F-score} = 2 \cdot \frac{\text{Precision} \cdot \text{Recall}}{\text{Precision} + \text{Recall}} \quad (7)$$

Additionally, we compute the mean absolute error (MAE) of the number of predicted PS

$$\text{MAE} = \frac{1}{N} \sum_{i=1}^N |\hat{n}_i - n_i| \quad (8)$$

where  $N$  is the number of dataset samples,  $n_i$  is the number of ground truth PS in the  $i$ -th sample, and  $\hat{n}_i$  is the number of predicted PS for the sample. The average Hausdorff distance  $d_{\text{AHD}}$  measures the distance between two point sets  $X$  and  $Y$ :

$$d_{\text{AHD}}(X, Y) = \frac{1}{2} \left( \frac{1}{|X|} \sum_{\vec{x} \in X} \min_{\vec{y} \in Y} \|\vec{x} - \vec{y}\| + \frac{1}{|Y|} \sum_{\vec{y} \in Y} \min_{\vec{x} \in X} \|\vec{x} - \vec{y}\| \right) \quad (9)$$

where  $|X|$  and  $|Y|$  are the number of points in  $X$  and  $Y$ , respectively and  $\|\cdot\|$  is the Euclidean distance. We report the mean average Hausdorff distance for PS predictions

$$\text{MAHD} = \frac{1}{N} \sum_{i=1}^N d_{\text{AHD}}(S_i, \hat{S}_i) \quad (10)$$

where  $S_i$  is the set of ground truth PS and  $\hat{S}_i$  is the set of predicted PS for sample  $i$ . If either  $S_i$  or  $\hat{S}_i$  is empty and the other set is not empty we set  $d_{\text{AHD}}(S_i, \hat{S}_i)$  to the image diagonal in pixels.

## 2.5. Smoothing and Interpolation

To be able to compare the CNN-based phase predictions shown in **Figure 10B** with results obtained with a reference method, we reconstructed or enhanced the noisy and/or sparse phase maps shown in **Figure 10C** using kernel-based spatio-temporal outlier filter, inpainting and smoothing techniques. The filtering techniques were also applied to experimental data (see **Figure 5A**) and section 2.2. The filtering is performed on trigonometrically encoded phase values, where each real-valued phase value in the video is converted into its complex decomposition:

$$\phi(x, y; t) \rightarrow \cos \phi(x, y; t) + i \cdot \sin \phi(x, y; t) \quad (11)$$

Spatio-temporal kernels are then used to average the complex phase values in space and over time in small disk-shaped sub-regions  $S_{d, \Delta t}$  with diameter  $d$  and with  $\Delta t = 3$  at times  $t - 1$ ,  $t$  and  $t + 1$ . In order to remove outliers in the experimental data and the noisy simulated data, the Kuramoto order parameter  $r(x, y; t)$  (Kuramoto, 1984) was computed in every pixel at every time step:

$$r \cdot e^{i\phi} = \frac{1}{N} \sum_i^N e^{i\phi_j} \quad (12)$$

where  $j = 1, \dots, N$  is the number of complex phase values within each kernel with diameter  $d = 5$  pixels and  $\Delta t = 3$ . Phase values were considered outliers if  $r < 0.9$  and accordingly removed, as shown in **Figure 5A**. Missing phase values were replaced with phase values averaged from surrounding phase values within the spatio-temporal kernel, given that at least 30% of the entries within the kernel were non-missing or valid phase entries. The process was repeated until the entire video was filled with valid phase entries. Lastly, the denoised, inpainted phase maps were smoothed averaging all phase values within a small spatio-temporal kernel typically with  $d = 7$  and  $\Delta t = 3$ , if not stated otherwise. In **Figure 10**, the noisy data was processed using the outlier and smoothing filters, the low resolution data was smoothed with  $d = 11$  pixels, the  $8 \times 8$  large and small grid data was inpainted 7 times with  $d = 11$  pixels, and the sparse grid data was inpainted 10 times with  $d = 19$  pixels, all with  $\Delta t = 3$ . With the sparse data the denoising was performed after inpainting and before smoothing.

## 3. RESULTS

We found that deep encoding-decoding convolutional neural networks (CNNs) can be used to compute phase maps and phase singularities (PS) from a short sequence of excitation wave patterns. The prediction of phase maps can be performed robustly and accurately ( $\sim 90 - 99\%$ ) with both experimental and simulated data, even with extremely noisy or sparse patterns (see **Figures 6–13** and **Supplementary Videos 1, 4–7**). Phase predictions remained accurate across different species, with models being trained on one species and then being successfully applied to another. Additionally, models that were trained solely on simulation data of VF could be applied to experimental

data, see **Figures 7, 8**. PS can be predicted either directly from excitation wave patterns or indirectly by first predicting phase maps from excitation wave patterns and then computing PS in the predicted phase maps. While in principle both direct and indirect PS prediction methods can determine the positions of PS very precisely (F-scores of  $\sim 97\%$ , see **Table 1**), direct PS predictions are very sensitive to noise and sparsity. Indirect PS predictions are far more robust. Accordingly, with the indirect PS prediction method we were able to locate PS in optical mapping recordings of VF sufficiently reliably and accurately, whereas with the direct PS prediction method this task was more challenging and produced only moderately successful results (see **Table 2**).

**Figures 6, 7** and **Supplementary Video 1** show predictions of phase maps when the neural network analyzes voltage-sensitive optical mapping videos showing action potential spiral vortex waves during ventricular fibrillation (VF) on the surface of rabbit and porcine hearts. **Figure 6A** shows raw pixel-wise normalized optical maps with a counter-clock-wise rotating action potential spiral vortex wave on the ventricular surface of an isolated pig heart (close-up,  $48 \times 48$  pixels cutout from original video image). The action potential rotor performs one rotation in about 110 ms. The phase maps in the second and third row in **Figure 6A** show the predicted phase maps  $\hat{\phi}$  obtained with model M1 and ground truth phase maps  $\phi$ , respectively. The action potential rotor is characterized by a pinwheel pattern in the phase maps, and the rotational core or PS is indicated by lines of equal phase which merge at the center of the pinwheel pattern. Predicted and ground truth phase maps are visually almost indistinguishable and exhibit only minor differences. The data was not seen by the neural network previously during training. The predicted phase maps are smooth even though the optical maps showing the action potential wave patterns are noisy. The neural network is able to predict more complicated wave patterns with multiple rotors or phase singularities (see **Figure 7** and **Supplementary Videos 1, 3**). The upper row in **Figure 7B** shows phase map predictions of an action potential figure-of-eight reentry pattern on the ventricular surface of a rabbit heart during VF. The predicted and ground truth phase maps shown in **Figure 7A** can only be distinguished from each other upon close inspection. Analyzing a short sequence of 10 optical maps, the neural network provides phase map predictions which are very accurate and sufficiently smooth in both space and over time, and the predictions can be retrieved in real-time at an acquisition speed of 500 fps. **Figure 6B** shows an optical trace of a series of action potentials and the corresponding time-series of the predicted phase, which was obtained from the sequence of predicted phase maps in **Figure 6A** using model M1. Even though each phase map was predicted independently at each time step, the time-course of the predicted phase signal  $\hat{\phi}(t)$  is relatively smooth, see **Supplementary Videos 1, 4–7** for an impression of the temporal smoothness of the predictions. On average, the accuracy of the phase prediction with model architecture M1 is  $97\% \pm 8\%$  or  $98\% \pm 6\%$  in terms of angular accuracy, if the model was trained on pig data and is evaluated on pig data or, alternatively, trained on rabbit data and evaluated on rabbit data (evaluation on  $\sim 5,000$  frames that were not part of the training data), respectively. We did not find a

significant difference in the accuracy between models M1, the LSTM model M2, or the U-Net model M3. For instance, when trained and evaluated on pig data, the angular accuracy for the phase prediction was  $96.5\% \pm 7.9\%$  for M1,  $96.1\% \pm 8.1\%$  for M2, and  $96.7\% \pm 7.8\%$  for model M3.

### 3.1. Phase Prediction Across Species and Dynamical Regimes

We found that phase prediction models that were trained on pig optical mapping data can also be applied to rabbit optical mapping data and achieve equally high phase prediction accuracies on the data ( $96.5\% \pm 7.9\%$  vs.  $97.0\% \pm 7.5\%$ ), see **Figure 8**. With such cross-species training, we observed higher accuracies when training from one species to another than vice versa (Rabbit→Pig:  $93.4\% \pm 12.2\%$  vs. Pig→Rabbit:  $97.0\% \pm 7.5\%$ ). This is presumably due to differences in the training data (more hearts, more diverse views in one species than the other). Surprisingly, we found that even models that were solely trained with simulation data, as shown in **Figure 4A**, can be used to predict phase maps of VF optical mapping data and that these models achieve acceptable results, see lower row in **Figures 7B, 8** (the simulation data was randomly masked with masks which were used with the experimental data (see **Supplementary Video 2**), all values outside the mask were set to 0). This demonstrates that the model can be applied to significantly different data than the data it was trained on. This

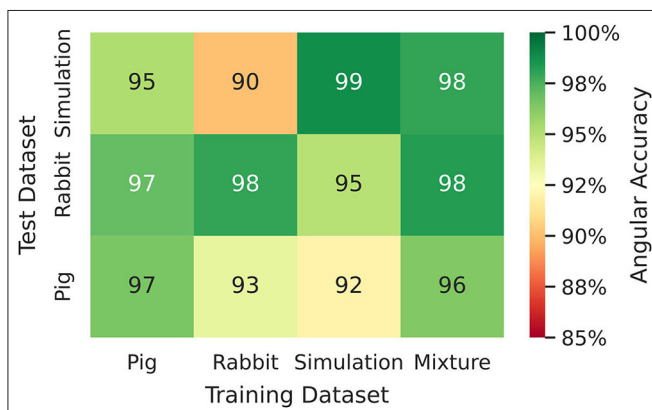


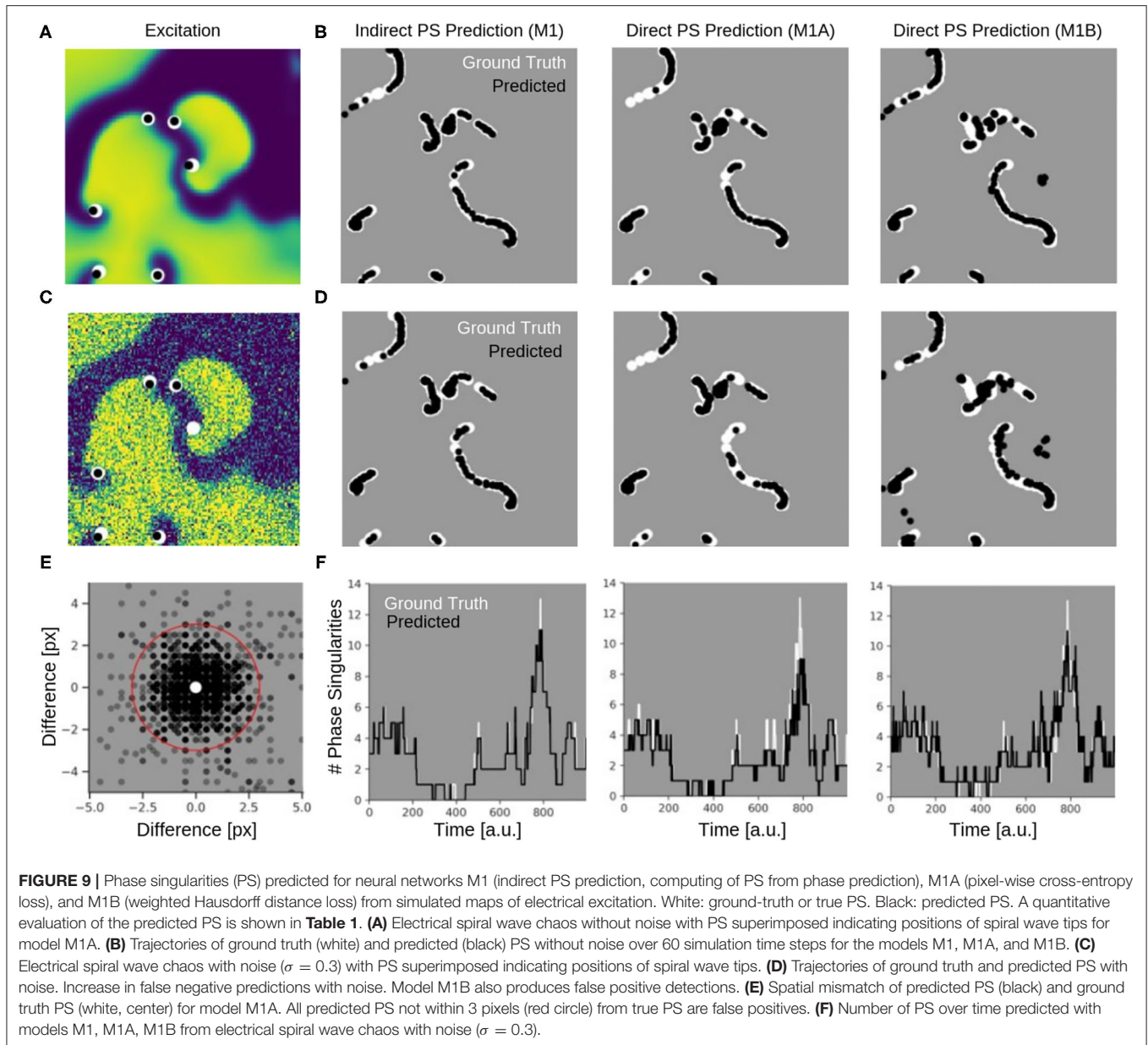
**FIGURE 8** | Phase prediction accuracies for neural network models trained on either pig, rabbit or simulation data, or a mixture of all data, cf. **Figure 4** and **Supplementary Video 2**. Prediction across species or from simulation to experiment with models trained on either one species and applied to another species or on simulation data and applied to rabbit or pig optical mapping data. All models were applied to test data consisting of 5,000 samples from experimental recordings or simulations, respectively. The prediction is most accurate when trained on the same data (Pig→Pig  $97\% \pm 8\%$ ; Rabbit→Rabbit  $98\% \pm 6\%$ ; Simulation→Simulation  $99\% \pm 4\%$ ). Nevertheless, the models appear to generalize as prediction across species is possible and achieves accuracies above 90% (Pig→Rabbit  $97\% \pm 8\%$ , Rabbit→Pig  $93\% \pm 13\%$ ). The pig training data is more diverse than the rabbit training data (more hearts and different views), which yields higher accuracies when predicting from pig to rabbit than vice versa. A model that was trained solely on simulation data can also be used to predict phase maps from experimental data (e.g., Simulation→Rabbit  $95\% \pm 10\%$ ).

also hints at the model generalizing and learning to associate phase maps with spatio-temporal dark-bright patterns in general rather than memorizing the particular wave dynamics. Note that the simulation data only includes two-dimensional wave dynamics, whereas the experimental data corresponds to three-dimensional wave dynamics which are observed on the surface. To our surprise, we found that models trained on simulation data without noise performed better on optical mapping data than when they were trained on simulation data with noise. The network performed equally well across the different dynamical regimes in the simulated data, which includes episodes with both more laminar and more chaotic spiral wave dynamics with longer and shorter wavelengths (see **Figure 4**). Lastly, **Figure 8** shows that a neural network that was trained on a mixture of pig, rabbit and simulation data provides consistently high phase prediction accuracies of 96 – 98% across all three datasets. Taken together, these results demonstrate that the phase prediction neural network can be applied to a wide range of VF dynamics with various wave lengths and frequencies. Note that the rabbit data contains VF episodes with and without Cromakalim, which modulates the dynamics significantly. While it was not possible to create sufficiently large rabbit training datasets to determine the performance during cross-training (without Cromakalim → with Cromakalim or vice versa), we did not notice a significant change in accuracy when evaluating the performance of a general rabbit model on sub-data types (without Cromakalim vs. with Cromakalim). The analysis was performed with model M1.

### 3.2. Phase Singularity Prediction

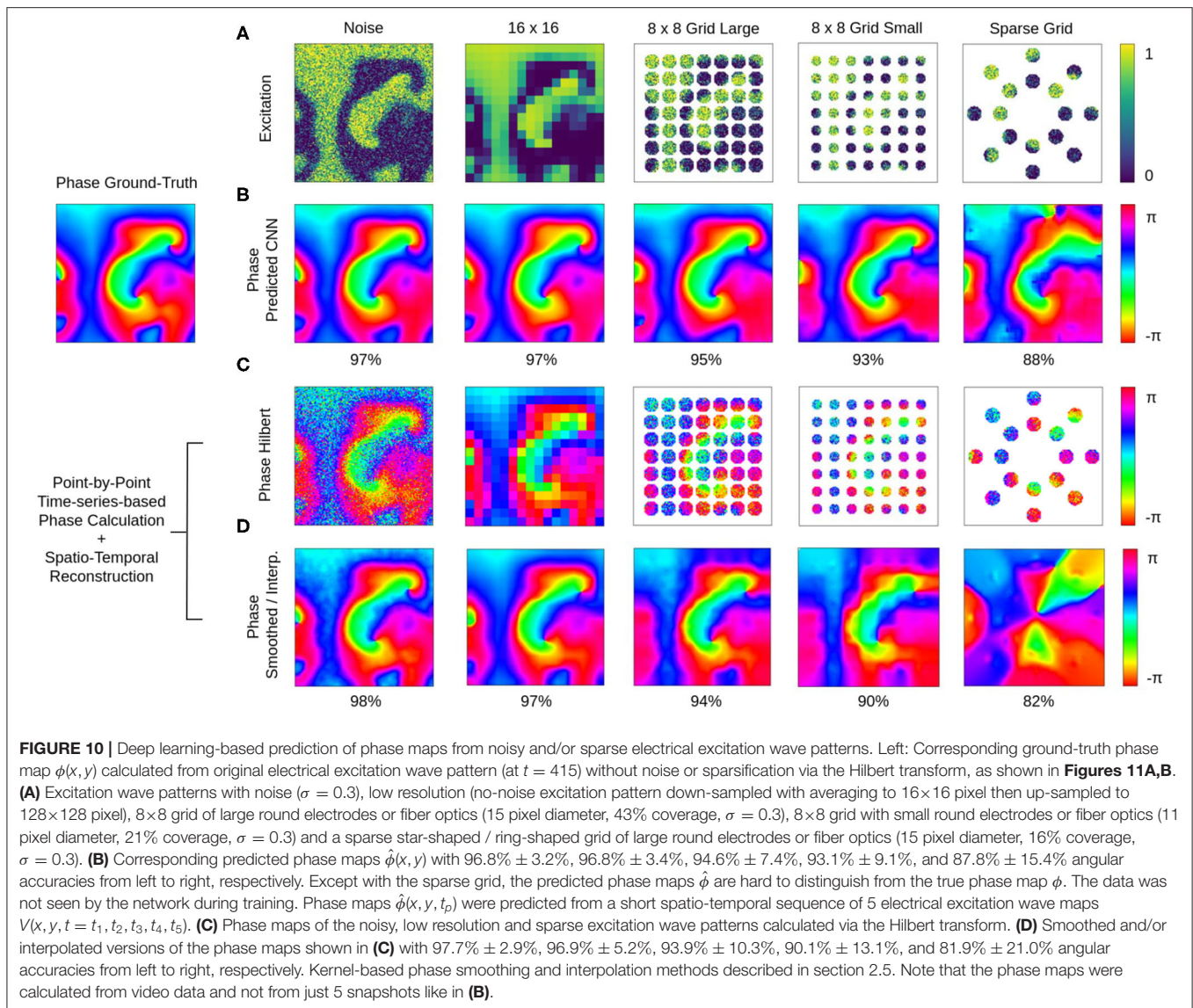
We found that the prediction of phase singularities (PS) from electrical excitation wave patterns was less accurate and less robust than predicting phase maps. This was especially true with challenging data, such as optical mapping recordings, or noisy and sparsified simulation data. Here, we compare three different neural network models M1, M1A, and M1B. Model M1 predicts PS indirectly by first predicting phase maps and subsequently calculating PS positions using the line integral technique. Models M1A and M1B both predict PS directly, where M1A uses a pixel-wise loss function and M1B uses a distance-based loss function during training, see section 2.1. Both models have different drawbacks: model M1A was better than M1B on simulation data both without and with noise (see **Table 1**), while M1B performs slightly better on optical mapping recordings than M1A (see **Table 2** and **Supplementary Video 3**). Model M1A is very conservative on challenging data, it occasionally produces false positives but mostly misses many true PS. Model M1B, on the other hand, is not as precise as M1A, and predicts more PS and produces more false detections. Overall, the indirect PS prediction using model M1 shows a far better performance than both direct methods with models M1A and M1B.

**Figure 9** shows the PS predictions on simulated spiral wave chaos data. **Figures 9A,C** show predicted PS (black) and ground truth (white) PS superimposed onto the corresponding electrical excitation wave maps (PS were predicted with model M1A). The maps demonstrate that both predicted and ground truth PS describe equally well the tips of spiral waves. However, with noise, one of the six PS was not detected by the neural network



(false negative detection). **Figures 9B,D** show the trajectories of the predicted (black) and ground truth (white) PS over a short time span (60 simulation time steps), without and with noise ( $\sigma = 0.3$ ), respectively, predicted indirectly with model M1 and directly with the models M1A and M1B. The predictions were obtained from a short sequence of  $N_t = 5$  excitation frames (c.f. **Figure 13A**). The trajectories co-align and demonstrate that PS are mostly predicted in locations where true PS are located. However, model M1B produces false positives even without noise. Moreover, all PS prediction models miss a portion of ground truth PS, and we counted these mispredictions as false negatives. **Figure 9E** shows the spatial distribution of mismatches between predicted and ground truth PS for model M1A with noise  $\sigma = 0.3$ , where the positions of the predicted PS are plotted

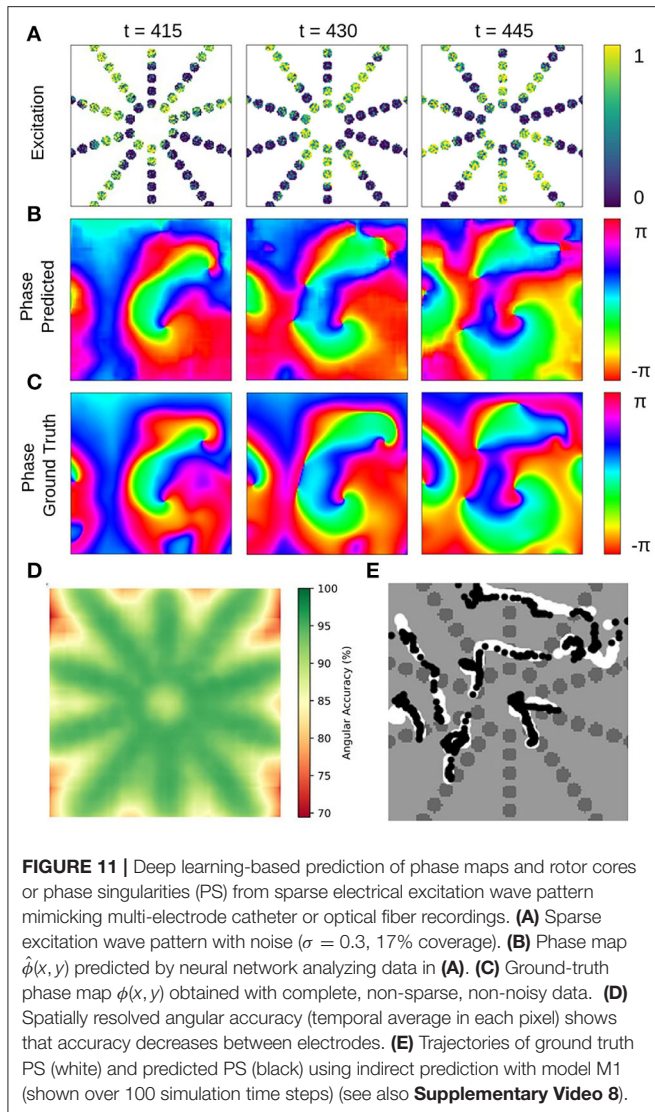
relative to the position of the ground truth PS at the center. All predicted PS which lie outside a radius of 3 pixels (red circle) from the ground truth PS are counted as false positives. The sub-pixel resolution accuracy of PS is a result of our method: we calculated PS positions from a series of pixels in the PS prediction image, see section 2.1. **Table 1** shows the evaluation of the PS prediction for all three models without and with noise in terms of precision, recall, F-score, MAE and MAHD on the test data consisting of 5,000 samples with 17,360 ground truth PS in total. Without noise model M1A is slightly better or equal to the indirect model M1 (e.g., F-score of 96.8 vs. 96.5%), while model M1B is significantly worse in all measures (F-score 86.5%). With noise however, the recall is significantly reduced for model M1A (85.9 vs. 96.4%, F-score 91.2%), as the number of false negative



predictions increases and the number of true positive predictions decreases (see **Figure 9D**). The number of false negatives does not increase, however, and the precision stays the same without and with noise with model M1A. This indicates that the model is rather conservative, insofar as when the difficulty for the model to predict PS locations increases it rather misses true PS instead of predicting false positives. This can also be seen in **Figure 9F**, which shows the number of predicted (black) and ground truth (white) PS over time for  $\sigma = 0.3$ .

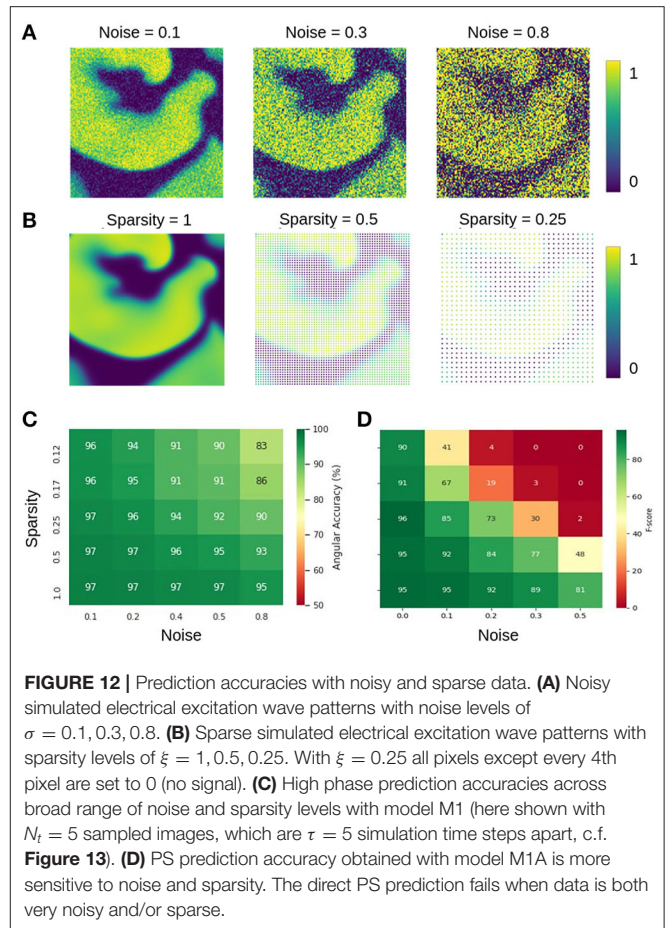
While the indirect PS predictions obtained with model M1 follow the ground truth PS closely, the direct PS predictions obtained with models M1A and M1B follow the trend overall but at times deviate considerably from the ground truth. Model M1A consistently underestimates the number of PS, whereas model M1B both under- and overestimates PS. **Supplementary Video 5** shows the PS predictions with model M1A for different simulated electrical excitation wave patterns without and with noise as well

as with sparsification. The conservatism of model M1A is caused by its pixel-wise loss function, which does not account for the distance between predicted PS locations and true PS positions unless the pixels overlap. The loss function is used during training to calculate an error value for every pixel of the predicted image of probable PS locations. As the likelihood of a pixel containing a PS is very small, there is a class imbalance (number of pixels with vs. without PS) for all pixel-wise loss functions and the network is biased toward not predicting a PS for challenging cases. Model M1B, on the other hand, uses a loss function which is directly based on the distance between predicted and ground truth PS locations. **Table 1** shows however, that model M1B is significantly less accurate for all measures than models M1 and M1A both with and without noise. **Figures 9B,D** show that M1B predicts false positives both without and with noise. In contrast, the indirect PS prediction with model M1 produces very few false positives, and the recall as well as the precision decrease only



moderately with the addition of noise resulting in an F-score of 94.6%. With regard to the direct PS prediction it is important to point out that the PS locations are determined by weighting multiple pixels, which surround the true PS and indicate probable PS positions (see **Figure 3C**). With model M1B this position estimation is especially problematic because a lot more pixels indicate the PS than with model M1A. Accordingly, two nearby PS are often not sufficiently resolved in the prediction image and cannot be separated, which then produces a false positive detection between two true PS. We tested different methods designed to extract individual PS positions as proposed by Ribera et al. (2019), but did not observe an improvement of the PS prediction performance with model M1B.

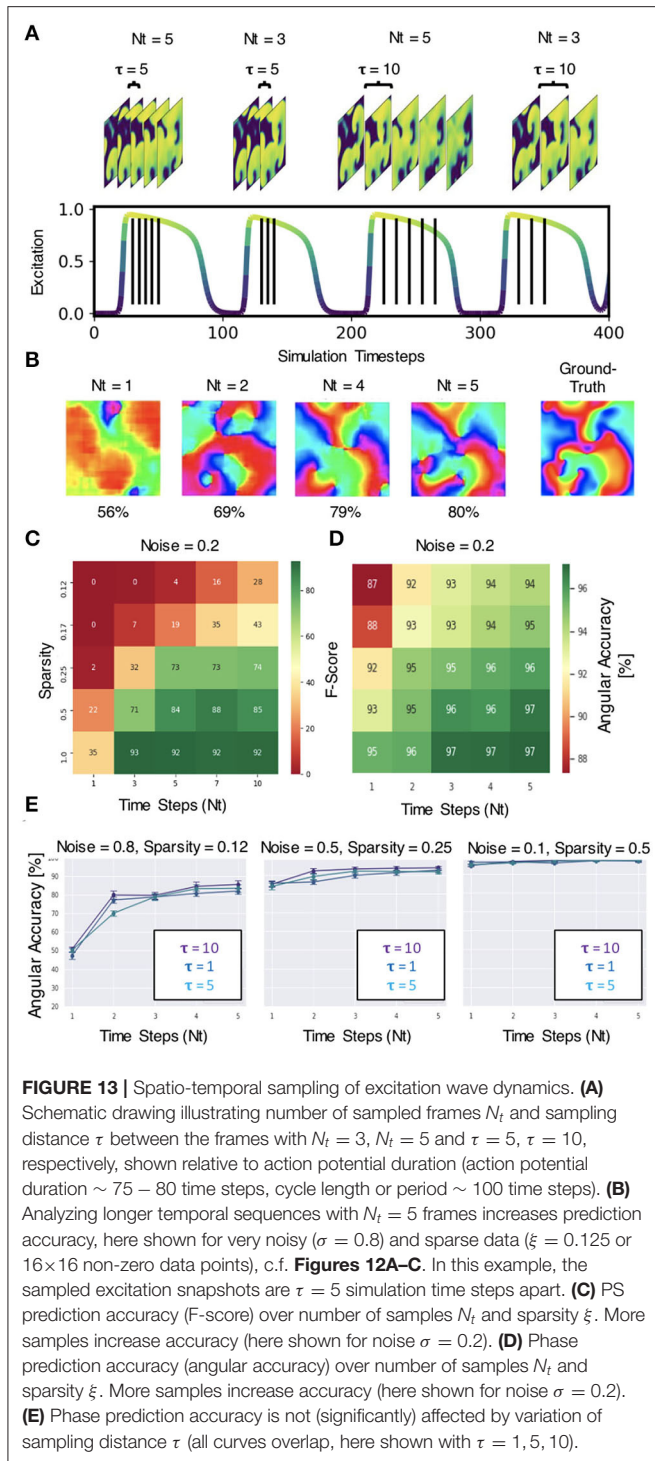
**Table 2** and **Supplementary Video 3** show PS predicted by the same models when trained and evaluated on rabbit optical mapping data (see also **Figure 4**). The indirect PS prediction with model M1 (F-score of 80.1%) is far more robust than and superior to the direct PS prediction with experimental data. We found that these indirectly predicted PS matched the dynamics of



the true PS computed from rabbit optical mapping data very well (see video). The direct prediction model M1A performs poorly (F-score of 11.8%), as it misses most true PS (recall 11.8%). However, it appears to predict some false positives mainly at the medium boundaries (see video). Model M1B achieves a significantly better F-score than model M1A of 42.5% on the optical mapping data, as it does not suffer from the conservatism exhibited by model M1A. However, overall, the performance of model M1B is still poor on optical mapping data.

### 3.3. Prediction of Phase Maps From Noisy, Low-Resolution or Sparse Excitation Wave Maps

The phase prediction neural network can predict phase maps even from very noisy, low-resolution and/or very sparse electrical excitation wave maps. **Figures 10, 11** and **Supplementary Videos 4, 6** show phase predictions obtained with model M1 with various simulated noisy, low-resolution or sparse excitation wave patterns, which are very generic simulations of imaging scenarios with low-resolution or low signal-to-noise sensors, multi-electrode arrays or (catheter) mapping electrodes, fiber optics or other similar sensors. **Figure 10A** shows exemplary snapshots of the excitation videos that were analyzed: (1) a noisy ( $\sigma = 0.3$ ) excitation pattern with

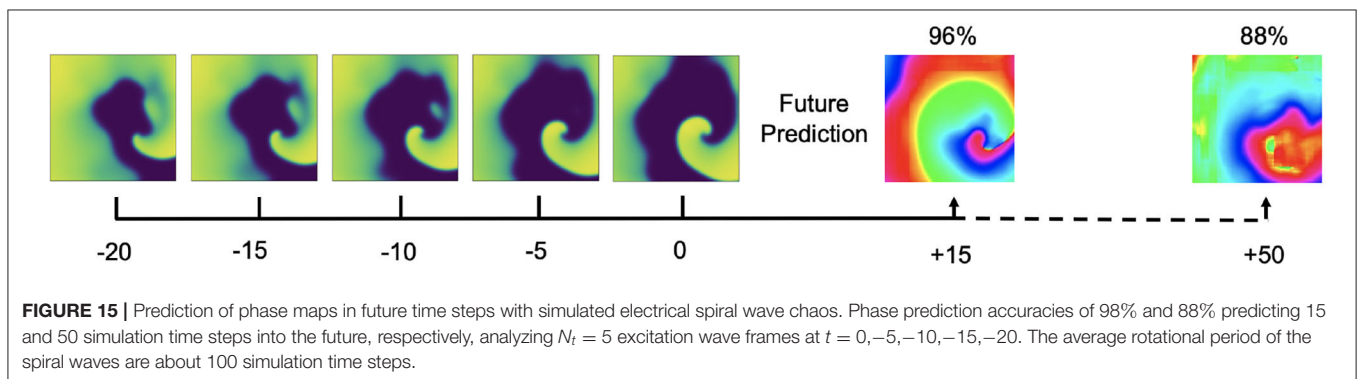
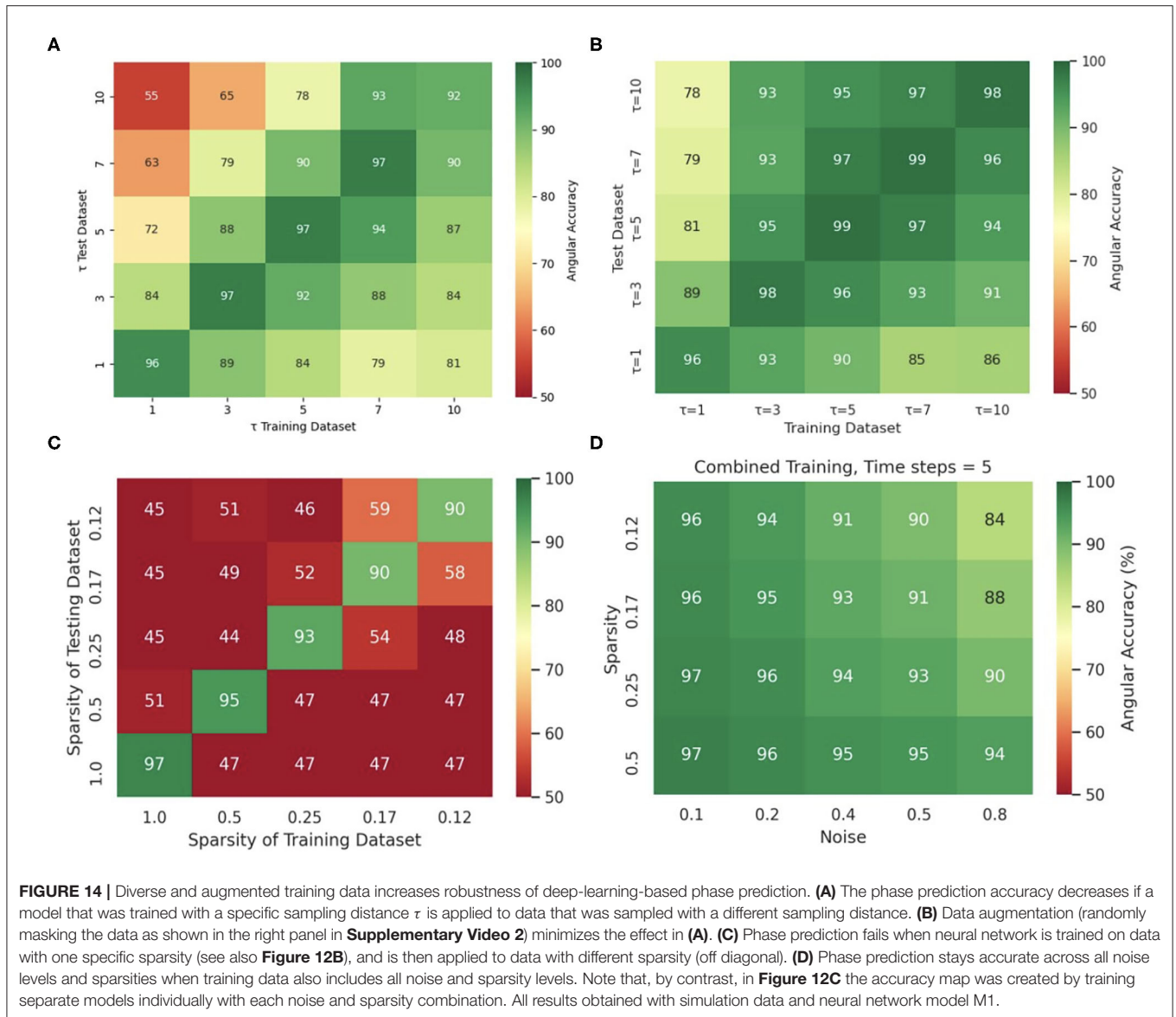


128×128 pixels resolution, (2) a low-resolution version of the same pattern that was derived by down-sampling the original non-noisy excitation pattern to 16×16 pixels resolution and then up-sampling the pattern without interpolation to 128×128 pixels resolution, (3) a 8×8 grid of large round electrodes or fiber optics 16 pixels apart with a diameter of 15 pixels each, the grid covering 43% of the area (with noise  $\sigma = 0.3$ ), (4) a 8×8 grid with small round electrodes or fiber optics 16 pixels apart with a diameter

of 11 pixels each, the grid covering 21% of the area (with noise  $\sigma = 0.3$ ), and (5) a sparse star-shaped / ring-shaped grid of large round electrodes or fiber optics with a diameter of 15 pixels each, the grid covering 16% of the area (with noise  $\sigma = 0.3$ ). **Figure 10A** shows the corresponding predicted phase maps  $\hat{\phi}$  predicted using the neural network model M1. The predicted phase maps  $\hat{\phi}$  are visually nearly indistinguishable from the ground truth phase map  $\phi$  shown as a reference on the left. The phase maps were predicted with angular accuracies of  $96.8\% \pm 3.2$ ,  $96.8\% \pm 3.4$ ,  $94.6\% \pm 7.4$ ,  $93.1\% \pm 9.1$ , and  $87.8\% \pm 15.4\%$  from left to right, respectively. The maps illustrate that the deep-learning-based phase prediction can suppress noise, enhance spatial resolution, and interpolate missing data and recover phase maps even when it only sees a fraction of the electrical data, as shown in the last example and in **Figure 11**.

The ground truth phase map  $\phi$  in **Figure 10** was computed from the original electrical excitation wave pattern without noise ( $\sigma = 0.0$ ) using the Hilbert transform, computing in each pixel  $(x, y)$  individually a phase signal from time-series data  $V(t)_{x,y} \rightarrow \phi(t)_{x,y}$  as shown in **Figure 1**. The phase maps shown in **Figure 10C** were equally computed pixel-by-pixel using the Hilbert transform, but were computed directly from the noisy, low-resolution or sparse electrical excitation data shown in **Figure 10A**. The phase maps accordingly include the same features, e.g., they include noise or remain sparse. The phase maps shown in **Figure 10D** were reconstructed from the noisy, low-resolution or sparse phase maps in **Figure 10C** using spatio-temporal inpainting and smoothing techniques, as described in section 2.5. They serve as a reference and allow the comparison of the deep learning with another interpolation method. While the reconstructed phase maps in **Figure 10D** also provide sufficiently accurate reconstructions with noise, low-resolution and low sparsity, with further increasing sparsity the reference method fails to produce accurate results and is outperformed by the deep learning-based phase prediction. Note that, even though the accuracy of both approaches are equally or comparably high, the reconstructed phase maps in **Figure 10D** contain noise or distortions, while the deep learning-based approach in **Figure 10B** produces consistently very smooth phase maps.

The neural network's ability to interpolate and reconstruct phase maps allows the tracking of PS between sensors even when they are relatively far apart (see **Figure 11** and **Supplementary Video 8**). **Figures 11A–C** show a sparse, star-shaped electrode/sensor configuration measuring an excitation wave pattern, and the resulting predicted and ground truth phase maps with this configuration, respectively. The predicted phase maps resolve the rotor dynamics very well, particularly toward the center where the electrode density is higher (average angular accuracy for entire field of view:  $\sim 91\%$ ). The average angular accuracy (temporal average in each pixel) resolved in space in **Figure 11D** indicates that the phase prediction accuracy remains sufficiently high between the electrodes toward the center. Accordingly, **Figure 11E** shows how the predicted PS (black) represent the ground truth PS (white) sufficiently well and follow their trajectories between and across electrodes (shown over 100 simulation time steps). The total area of the sensor/electrodes covers only 17% of the entire 2D simulation domain.



### 3.4. Extreme Sparsity and Noise

The data shown in **Figure 12** characterizes the phase and PS prediction performance with extreme noise and sparsity in

more detail. **Figure 12A** shows maps with simulated electrical excitation wave patterns with noise levels of  $\sigma = 0.1, 0.3, 0.8$ , and **Figure 12B** shows the same simulated electrical excitation



**TABLE 1** | Evaluation of phase singularity (PS) prediction on simulated electrical spiral wave chaos without ( $\sigma = 0$ ) and with noise ( $\sigma = 0.3$ ) for the different models M1, M1A, M1B.

Model	M1		M1A		M1B	
	$\sigma = 0$	$\sigma = 0.3$	$\sigma = 0$	$\sigma = 0.3$	$\sigma = 0$	$\sigma = 0.3$
Noise						
Precision	97.2 %	96.2 %	97.2 %	97.2 %	86.7 %	82.1 %
Recall	95.7 %	93.1 %	96.4 %	85.9 %	86.4 %	84.3 %
F-score	96.5 %	94.6 %	96.8 %	91.2 %	86.5 %	83.1 %
MAE	0.2	0.2	0.2	0.5	0.4	0.5
MAHD	2.3 px	3.1 px	2.0 px	5.0 px	4.0 px	6.6 px
MAHD*	1.4 px	1.8 px	1.4 px	3.1 px	2.4 px	3.6 px

PS predictions were performed from 5 excitation frames and are shown in **Figure 9**. MAE is the mean absolute error of the number of predicted PS, MAHD is the mean average Hausdorff distance. The test dataset contains 5,000 frames with 17,360 PS in total, however 420 frames contain no ground truth PS. If the model predicts any PS for a frame which contains no ground truth PS—or if no PS are predicted for a sample which does contain ground truth PS—we assign a maximum average Hausdorff distance (181 px) for the computation of the MAHD. This skews the MAHD significantly. Accordingly, MAHD\* is the MAHD when we ignore these samples.

**TABLE 2** | PS prediction with models M1 (indirect from phase), M1A (pixel-wise loss), and M1B (distance-based loss) when trained and evaluated on rabbit optical mapping data using a radius of  $r = 6$  px for computation of precision, recall, and F-score.

Model	Precision (%)	Recall (%)	F-score (%)	MAE	MAHD
M1	82.9	77.5	80.1	0.7	11.6
M1A	41.9	11.8	18.4	2.2	113.6
M1B	40.4	44.9	42.5	1.4	24.8

**Supplementary Video 3** shows the predicted PS for all three models. The indirect PS estimation (M1) is far more accurate than the direct PS prediction (M1A and M1B).

wave patterns without noise but sparsified with sparsity levels of  $\xi = 1.0, 0.5, 0.25$ . The excitation images were sparsified by setting all pixels except every  $n$ -th pixel in  $x$ - and  $y$ -direction to 0 (no signal). Accordingly, a sparsity level of  $\xi = 0.25$  corresponds to setting every pixel but every 4th pixel to 0, for instance. **Figures 12C,D** show the prediction accuracies obtained with different combinations of noise and sparsity for the phase prediction with model M1 (angular accuracy) and for the PS prediction with model M1A (F-score), respectively. The individual prediction accuracies were obtained when training was performed with each specific combination of  $\sigma$  and  $\xi$ . The map in **Figure 12C** shows that the phase prediction with model M1 is highly accurate and remains above 90% angular accuracy over a wide range of noise and sparsity levels. In particular, with non-sparse data ( $\xi = 1.0$ ), the angular accuracy stays above 95% with noise levels of up to  $\sigma = 0.8$ , which corresponds to the noise level shown on the right in **Figure 12A**. With  $\xi = 0.125$  sparsification, the information in the image is reduced to  $16 \times 16 = 256$  non-zero pixels instead of  $128 \times 128 = 16,384$  pixels. Therefore, the neural network can analyze only less than 2% of the image. Despite this reduction, the network provides accuracies of 94–97% with noise levels of  $\sigma = 0.1$ –0.2 (and at least 90% with noise levels of up to  $\sigma = 0.5$ ). While the phase prediction is accurate over a broad range of noise and sparsity levels, **Figure 12D** shows that the direct prediction of PS using model M1A is less accurate and robust against noise or sparsity. The F-score stays above 90% only at low noise or

sparsity levels and deteriorates quickly when both increase (e.g., sparsity  $\xi = 0.25$  and noise  $\sigma = 0.3$ ). The F-score even drops entirely to 0% in extremely noisy and sparse regimes. The systematic analysis in **Figure 12D** confirms the impression given in **Figures 9C,D** that the predicted PS trajectories frequently contain false detections when predicted directly. The angular accuracies and F-scores were computed over the testing dataset with 5,000 frames. The data shows that even though noise and sparsity impair the phase prediction accuracy, overall the phase predictions remain, in contrast to the PS prediction, robust and sufficiently accurate in the presence of strong noise and with extreme sparsity. Autoencoder neural networks have excellent denoising capabilities and are very effective at interpolating image data (Vincent et al., 2008; Gondara, 2016), and this property can be observed at work in **Figures 6, 10–12**.

### 3.5. Spatio-Temporal Sampling Over Spiral Wave's Period Increases Prediction Accuracy

The neural network does not require very much information to be able to predict phase maps or phase singularities (PS). A short sequence of  $N_t = 5$ –10 excitation wave patterns is sufficient in most situations to make accurate predictions, even with extreme noise and/or sparsity, as shown in **Figure 12**. The results in **Figures 6–12** were obtained with either  $N_t = 5$  or  $N_t = 10$  excitation frames with simulated or experimental data, respectively. The number of sampled frames  $N_t$  and the sampling distance  $\tau$ , which corresponds to the temporal offset between the samples (see sketch in **Figure 13A**), are the two main parameters determining the phase and PS prediction accuracy.

Regarding the number of sampled frames  $N_t$ , we found that the predictions become more accurate when sampling the activity with more frames, but the accuracy does not improve significantly further with more than 5–10 frames. Analyzing a short spatio-temporal sequence ( $N_t = 4, 5, \dots, 10$ ) rather than just a single, static ( $N_t = 1$ ) excitation wave pattern or a few ( $N_t = 2, 3$ ) excitation wave patterns does not only increase the accuracy, but also improves the prediction robustness and ensures that the neural network is able to make predictions at

all in difficult environments with high noise or sparsity (see **Figures 13B–D**). **Figure 13B** shows how the prediction fails entirely if the network only analyzes 1 frame, but becomes progressively better with each frame and finally succeeds to produce satisfactory phase predictions (80%) when it analyzes a short sequence of  $N_t = 2, 4, 5$  frames. In this example, the phase map was predicted from a very noisy ( $\sigma = 0.8$ ) and very sparse ( $\xi = 0.125$ ) excitation pattern. The data demonstrates that the neural network is able to compensate information that is lacking in space with additional information it retrieves over time. The multi-frame analysis can also slightly improve the neural network's prediction accuracy when it already achieves high accuracies in less extreme conditions. **Figure 13C** shows that the F-score increases from 22% to about 85% when using  $N_t = 1, 3, 5, 7, 10$  frames for the direct PS prediction with model M1A. **Figure 13D** shows that the angular accuracy increases slightly from 93% to 97% when using  $N_t = 1, 2, 3, 4, 5$  frames for the phase prediction with model M1 with low sparsity ( $\xi = 0.5$ ) and low noise ( $\sigma = 0.2$ ). The PS prediction benefits more from the multi-frame analysis as it is more sensitive to noise and sparsity.

Regarding the sampling distance  $\tau$ , we made the following observations: (1) With experimental data, we were able to mix the rabbit, pig and simulation data and even though  $\tau$  was not perfectly adjusted to all of the different dominant frequencies of the wave dynamics or imaging speeds, the network was able to produce accurate predictions across all data (see **Figure 8**). We chose a sampling distance of  $\tau = 12$  ms for both the rabbit and pig data, resulting in an effective framerate of 83 fps. With  $N_t = 10$  the series of sampled frames covered 75–140% of the cycle length or dominant period of the VF dynamics (about 90–170 ms). The phase prediction failed with the experimental data when we used shorter sampling times  $T_\tau = \tau \cdot N_t$ , which covered only a smaller fraction of the cycle length (e.g., 15%). (2) With the simulation data shown in **Figure 4A**, the sampling distance  $\tau$  did not affect the phase prediction accuracy at all, and we achieved high accuracies even with short sampling times  $T_\tau$  (e.g., 5% with  $N_t = 5$  and  $\tau = 1$ ). **Figure 13E** shows that the angular accuracy does not change significantly when the sampling distance is varied ( $\tau = 1, \tau = 5$ , or  $\tau = 10$  with  $N_t = 5$  frames, shown for 3 different noise and sparsity levels). With these parameters, the dynamics are sampled over 5, 25, or 50 simulation time steps, which corresponds to about 5, 25, or 50% of the average cycle length or dominant period of the spiral wave dynamics of about 100 simulation time steps, respectively.

### 3.6. Training Data Diversity Increases Robustness Against Varying Imaging Parameters

Training the neural network with more diverse data broadens the distribution of data it can analyze and will prevent eventual overfitting to a particular feature in a dataset. The network's insensitivity to the sampling distance  $\tau$  with the simulation data, as discussed in section 3.5 and shown in **Figure 13E**, is an indication for overfitting when training and predicting solely on simulation data, because the same model

trained with and applied to optical mapping data is unable to produce correct predictions with short  $\tau$ . The different behavior with simulation and experimental data suggests that the network specializes with the simulation data in memorizing the dynamics based on instantaneous features (moving wavefronts etc.). However, this approach fails with experimental data, in which case it only succeeds if it is provided information that was sampled over a significant portion or the entire period of the reentry pattern. Interestingly, we also made the following observation: **Figure 14C** shows that the phase prediction accuracy drops if training was performed on the simulation data with just one specific sampling distance  $\tau_{train}$  and the network is then applied to data that was sampled with a different sampling distance  $\tau \neq \tau_{train}$ . Importantly, the analysis was performed on the simulation data without data augmentation, as shown in **Figure 4A** (with  $\sigma = 0$ ,  $\xi = 1$ ). However, **Figure 4D** shows that if the same simulation data is augmented with the masks shown in **Figure 4B**, see also **Supplementary Video 2**, then the network performs better and achieves higher accuracies at other sampling distances  $\tau$  even though it was not trained on these  $\tau$  values. For instance, if the network was trained with  $\tau_{train} = 5$  and achieves an accuracy of 99% at  $\tau = 5$ , it still achieves an accuracy of 96–97% with  $\tau = 3$  or  $\tau = 7$  just because the input data was augmented and includes other features (arbitrary masked regions) than just the wave dynamics on a square simulation domain. These findings are consistent with the finding that a single  $\tau$  could be used with a mix of experimental and simulated data, as described in section 3.1.

Similarly, **Figure 14C** shows that if the neural network is trained solely with a particular sparsification, for instance with  $\xi = 0.25$ , then it excels at performing predictions with  $\xi = 0.25$ , but fails with different sparsifications. Accordingly, the phase prediction only succeeds when the sparsity of the testing dataset matches the sparsity during training (along the diagonal), and fails when the sparsities in the training and testing datasets are different (off the diagonal). However, this issue can be resolved by training the network with data that includes all sparsifications (here  $\xi = 1.0, 0.5, 0.25, 0.17, 0.125$ ). **Figure 14D** shows that the same neural network can be applied to arbitrary noise and sparsification levels and will consistently yield phase prediction accuracies above 90% when the training was performed with data that contained all noise and sparsification levels. By contrast, in **Figure 12C** the training was performed individually with each specific combination of noise and sparsification. The broader training in **Figure 14D** makes the network more robust and yields just as high phase prediction accuracies as with each individual specialized training in **Figure 12C**.

The anecdotal findings in **Figures 8, 14** are representative of a very general property of neural networks and data driven approaches. Similar observations would be made with other parameters, such as noise, blurring or arbitrary sparsification patterns and we made very similar observations in a previous study (Christoph and Lebert, 2020) with an architecturally very similar neural network.

### 3.7. Predicting Future Phase Maps or PS Positions

It is possible to predict phase maps and PS positions in future time steps, but only within the immediate future. **Figure 15** shows predictions of phase maps with simulated spiral wave chaos, which the neural network M1 predicted 15 and 50 simulation time steps into the future. The network analyzed  $N_t = 5$  excitation wave frames at  $t = 0, -5, -10, -15, -20$  to make each phase prediction and achieved  $97.6\% \pm 2.5$ ,  $96.0\% \pm 3.4$ ,  $95.5\% \pm 4.1$ , and  $87.7\% \pm 17.6\%$  angular prediction accuracy 5, 10, 15, and 50 simulation time steps into the future, respectively. As the average cycle length or rotational period of the activity is about 100 simulation time steps, this corresponds to about half a rotation within which the prediction yet achieves satisfactory accuracies and about 1/5 of a rotation within which the prediction achieves very good accuracies.

## 4. DISCUSSION

We demonstrate that deep neural networks can be used to compute phase maps and locate the position of phase singularities (PS) when analyzing cardiac excitation wave dynamics. PS can be predicted by deep neural networks either directly from excitation wave patterns or indirectly by predicting first phase maps from the excitation wave patterns and then calculating PS in the predicted phase maps using classical techniques (e.g., the circular line integral method, shown in **Figure 1C**). This latter step is possible because the predicted phase maps are smooth. We found that the direct PS prediction was less robust than the prediction of phase maps, particularly with challenging data, and, accordingly, we only succeeded to reliably predict PS positions in experimental data with the indirect method. Predictions of phase maps and PS can be performed almost instantaneously from a short temporal sequence consisting of 1–10 snapshots of cardiac excitation waves. We successfully applied this deep learning-based rotor localization and phase mapping technique to both simulated and *ex-vivo* optical mapping data of ventricular fibrillation (VF), and we expect that the technique can also be applied to catheter mapping data of cardiac arrhythmias in clinical patients.

A critical issue in the use of neural networks lies in ensuring that the networks “generalize”. Neural networks are known to perform very well when applied to data that is very similar to, or “within the distribution,” of the training data, but their accuracy and robustness can quickly deteriorate when applied to other, less similar “out-of-distribution” data. Our results demonstrate that our deep learning-based phase mapping algorithm can be developed in one species and then applied to another species. We even show that the phase mapping algorithm can be developed with synthetic data generated in computer simulations and then applied to experimental data. This latter observation is particularly noteworthy in that the simulation data used to train the network was 2D, whereas the experimental data to which it was applied were surface observations of 3D dynamics. These findings suggest that the algorithm is able to learn the relevant correlation between patterns in a specific distribution of data, and

then extrapolate this mapping to differently distributed data that is well outside of the training distribution. From our results it appears that the deep learning algorithm learns to associate phase patterns with a broad class of excitable spatio-temporal activity, and understands the more generalized phase mapping problem, independent of physiological parameters or species-dependent wave dynamics.

Based on these findings, we anticipate that it will be possible to develop a similar deep learning-based phase mapping approach for clinical mapping of arrhythmias in human patients. Neural networks can in principle analyze any data, and they will likely be able to predict phase maps from extracellular field potential or electrogram measurements, just as they are able to predict phase maps from optical measurements of the cellular transmembrane potential. Because neural networks excel at detecting hidden patterns in data, “ignoring” noise, interpolating missing data, and enhancing spatial resolution, all of which they can do simultaneously, they are ideally suited for the analysis of catheter mapping data of atrial fibrillation. The application of such a deep learning-based algorithm would not only be restricted just to phase mapping, but could in principle also be extended to map any other characterizing feature of arrhythmias (e.g., activation or conduction velocity maps). As our results indicate, neural networks would be able to integrate sparse data acquired with multi-electrode basket catheters, given that they are trained with adequate high-resolution imaging data, which could be generated *ex vivo* or in computer simulations. Ultimately, deep-learning has great potential to alleviate some of the shortcomings of catheter mapping, which are largely associated with limited spatial resolution and interpolation artifacts (Martinez-Mateu et al., 2018; Van Nieuwenhuysse et al., 2021), that in turn can lead to misrepresentations of rotor dynamics and fibrillatory wave patterns during atrial fibrillation.

Other advantages of our technique are (i) that it can compute phase maps and PS in real-time with data that was acquired over a brief interval and (ii) that it can obviate pre-processing of the raw data (e.g., spatio-temporal smoothing and outlier removal). The predictions do not require the collection of long time-series, can be performed within one rotational period of the wave dynamics (see **Figure 13A**), and can be calculated in real-time at 500–1,000 fps using GPU hardware (at  $128 \times 128$  pixels resolution). Predictions can furthermore be performed into the immediate future, enabling predictions of PS positions within about the next 1/4 rotation of reentrant wave dynamics (see **Figure 15**). The latter aspect ii) makes the technique ideal for the processing of very noisy video data or data containing artifacts, such as motion artifacts. This could also make it an attractive phase mapping approach in other fields beyond cardiovascular research, for instance, when studying the dynamics of excitation waves and topological defects in other biological systems (Huang et al., 2010; Taniguchi et al., 2013; Tan et al., 2020; Liu et al., 2021). We expect that deep learning-based phase mapping can be applied to various forms of data. However, it should be noted that each application may require its own specialized training dataset and specific deep learning algorithm, despite the ability of these algorithms to generalize. The routine use

of the technique across many different laboratories will likely only be achieved with much larger and more diverse training datasets (including various species and experimental conditions). Further, neural networks are not a filtering technique *per se*, and will only be able to perform a particular task (e.g., denoising) if they are trained on adequate data. In future applications it will be crucial that training data includes the features, which are necessary for the neural network to learn the desired tasks. While we provided a proof-of-concept, we also acknowledge that there is still potential for improving the phase mapping and direct PS prediction overall, especially for use with experimental data. We found that the direct PS prediction was more sensitive to challenging data than the prediction of phase maps, especially with optical mapping data or noisy and sparsified simulation data. We anticipate that better direct PS predictions or even higher phase mapping accuracies could be achieved with both more and better training data and more advanced neural network architectures. We aim to address these issues in future research.

## 5. CONCLUSIONS

We demonstrated that convolutional neural networks can be used to predict phase maps and rotor core positions or phase singularities (PS) of reentrant cardiac excitation wave dynamics in both voltage-sensitive optical maps of ventricular fibrillation and simulated data mimicking low-resolution and/or sparse multi-electrode mapping data. The predictions can be made almost instantaneously, robustly and with accuracies of about 95%, and can be performed even in the presence of strong noise and highly sparse or incomplete data. Neural networks used for phase mapping of cardiac excitation waves are able to analyze data obtained in one species, even if they were trained on a different species, and can predict phase maps and PS with experimental data, even if they were trained solely with simulated data of electrical spiral wave chaos. In the future, our approach could be used in electro-anatomic mapping applications for the diagnosis of atrial fibrillation.

## DATA AVAILABILITY STATEMENT

The raw data and source code supporting the conclusions of this article will be made available by the authors upon reasonable request.

## ETHICS STATEMENT

All experiments conformed to the current Guide for Care and Use of Laboratory Animals, published by the National Institutes of Health (NIH Publication No. 85-23, revised 1996) and were approved by the Office of Research and Integrity Assurance at Georgia Institute of Technology.

## AUTHOR CONTRIBUTIONS

JL and JC conceived the research and implemented the algorithms. JL, NR, and JC conducted the data analysis and designed the figures. FHF performed the experiments and provided the experimental data. JL, FHF, and JC discussed the results and wrote the manuscript. All authors contributed to the article and approved the submitted version.

## FUNDING

This research was funded by the University of California, San Francisco. NR was a research Fellow supported by the Sarnoff Cardiovascular Research Foundation. FHF acknowledges support from NSF 2037894 and NIH 1R01HL143450.

## SUPPLEMENTARY MATERIAL

The Supplementary Material for this article can be found online at: <https://www.frontiersin.org/articles/10.3389/fphys.2021.782176/full#supplementary-material>

**Supplementary Video 1** | Neural network predictions of phase maps from voltage-sensitive optical mapping video data. The recording shows action potential spiral vortex waves during ventricular fibrillation on the left ventricular surface of a porcine heart, see also **Figure 6**. The pixel-wise normalized transmembrane voltage is shown on the left (yellow: depolarized, blue: repolarized tissue). Center: smoothed ground truth phase map, which was obtained from the noisy optical maps using the Hilbert transform, see **Figure 5A** and section 2.2. Right: phase map predicted by the neural network.

**Supplementary Video 2** | Comparison of the neural network input images for the prediction of a single phase map for the pig, rabbit, and simulation datasets used in **Figures 7, 8**. The video shows the  $N_t = 10$  images given as input to the neural network to predict a single phase map for each type of dataset.

**Supplementary Video 3** | PS prediction for rabbit optical mapping data using neural network models M1 (**left**), M1A (**middle**), M1B (**right**). The PS for model M1 are predicted indirectly by first predicting phase maps then computing PS in the phase maps using the circular line integration method.

**Supplementary Video 4** | Phase maps predicted by the neural network from (sparse) simulated electrical excitation wave maps without and with noise ( $\sigma = 0.3$ ). **Left**: electric excitation wave maps uses as network input ( $N_t = 5$ ). **Center**: ground truth or true phase. **Right**: neural network output.

**Supplementary Video 5** | Phase singularities (PS) predicted by the neural network M1A from (sparse) simulated electrical spiral wave chaos without and with noise ( $\sigma = 0.2$ ) for  $N_t = 5$ . **Left**: ground truth electrical excitation, **Center**: network input, **Right**: predicted PS (black) and true PS (white) superimposed onto the corresponding electrical excitation wave maps.

**Supplementary Video 6** | Phase maps predicted by the neural network from (sparse) simulated electrical excitation wave maps without and with noise ( $\sigma = 0.3$ ) for  $N_t = 5$ .

**Supplementary Video 7** | Neural network prediction of a single phase map. The 5 noisy and sparse electrical wave frames given as input to the neural network, as well as the predicted phase map and the true phase map are shown.

**Supplementary Video 8** | PS prediction using model M1 for the sparse and noisy excitation patterns shown in **Figure 11**. The predicted PS are shown in red, the ground truth in white. **Left**: The sparse excitation wave pattern with noise used as neural network input. **Right**: Ground truth excitation with sparsification shown in black.

## REFERENCES

- Abad, R., Collart, O., Ganesan, P., Rogers, A. J., Alhuseini, M. I., Rodrigo, M., et al. (2021). Three dimensional reconstruction to visualize atrial fibrillation activation patterns on curved atrial geometry. *PLoS ONE* 16 e0249873. doi: 10.1371/journal.pone.0249873
- Abadi, M., Agarwal, A., Barham, P., Brevdo, E., Chen, Z., Citro, C., et al. (2015). *TensorFlow: Large-Scale Machine Learning on Heterogeneous Systems*. Available online at: tensorflow.org.
- Alhuseini, M. I., Abuzaid, F., Rogers, A. J., Zaman, J. A., Baykaner, T., Clopton, P., et al. (2020). Machine learning to classify intracardiac electrical patterns during atrial fibrillation. *Circ. Arrhythmia Electrophysiol.* 13:e008160. doi: 10.1161/CIRCEP.119.008160
- Aliev, R. R., and Panfilov, A. V. (1996). A simple two-variable model of cardiac excitation. *Chaos Solitons Fractals* 7, 293–301. doi: 10.1016/0960-0779(95)00089-5
- Aronis, K. N., Berger, R. D., and Ashikaga, H. (2017). Rotors. *Circ Arrhythmia Electrophysiol.* 10:e005634. doi: 10.1161/CIRCEP.117.005634
- Barkley, D., Kness, M., and Tuckerman, L. S. (1990). Spiral-wave dynamics in a simple model of excitable media: the transition from simple to compound rotation. *Phys. Rev. A* 42, 2489–2492. doi: 10.1103/PhysRevA.42.2489
- Bray, M.-A., Lin, S.-F., Aliev, R. R., Roth, B. J., and Wikwso, J. P. Jr. (2001). Experimental and theoretical analysis of phase singularity dynamics in cardiac tissue. *J. Cardiovasc. Electrophysiol.* 12, 716–722. doi: 10.1046/j.1540-8167.2001.00716.x
- Bray, M.-A., and Wikwso, J. P. (2002). Considerations in phase plane analysis for nonstationary reentrant cardiac behavior. *Phys. Rev. E* 65:051902. doi: 10.1103/PhysRevE.65.051902
- Bursac, N., Aguel, F., and Tung, L. (2004). Multiarm spirals in a two-dimensional cardiac substrate. *Proc. Natl. Acad. Sci. U.S.A.* 101, 15530–15534. doi: 10.1073/pnas.0400984101
- Christoph, J., Chebbok, M., Richter, C., Schröder-Schetelig, J., Bittihn, P., Stein, S., et al. (2018). Electromechanical vortex filaments during cardiac fibrillation. *Nature* 555, 667–672. doi: 10.1038/nature26001
- Christoph, J., and Lebert, J. (2020). Inverse mechano-electrical reconstruction of cardiac excitation wave patterns from mechanical deformation using deep learning. *Chaos Interdiscipl J Nonlinear Sci.* 30:123134. doi: 10.1063/5.0023751
- Christoph, J., and Luther, S. (2018). Marker-free tracking for motion artifact compensation and deformation measurements in optical mapping videos of contracting hearts. *Front. Physiol.* 9:1483. doi: 10.3389/fphys.2018.01483
- Clayton, R., Zhuchkova, E., and Panfilov, A. (2006). Phase singularities and filaments: Simplifying complexity in computational models of ventricular fibrillation. *Prog. Biophys. Mol. Biol.* 90, 378–398. doi: 10.1016/j.pbiomolbio.2005.06.011
- Entcheva, E., and Bien, H. (2006). Macroscopic optical mapping of excitation in cardiac cell networks with ultra-high spatiotemporal resolution. *Prog. Biophys. Mol. Biol.* 92, 232–257. doi: 10.1016/j.pbiomolbio.2005.10.003
- Fenton, F., and Karma, A. (1998). Vortex dynamics in three-dimensional continuous myocardium with fiber rotation: filament instability and fibrillation. *Chaos Interdiscipl. J. Nonlinear Sci.* 8, 20–47. doi: 10.1063/1.166311
- Gondara, L. (2016). Medical image denoising using convolutional denoising autoencoders. *arXiv preprint arXiv:1608.04667v04662*. doi: 10.1109/ICDMW.2016.0041
- Gray, R. A., Pertsov, A. M., and Jalife, J. (1998). Spatial and temporal organization during cardiac fibrillation. *Nature* 392, 75–78. doi: 10.1038/32164
- Guillem, M. S., Climent, A. M., Rodrigo, M., Fernandez-Aviles, F., Atienza, F., and Berenfeld, O. (2016). Presence and stability of rotors in atrial fibrillation: evidence and therapeutic implications. *Cardiovasc. Res.* 109, 480–492. doi: 10.1093/cvr/cv011
- Gurevich, D. R., and Grigoriev, R. O. (2019). Robust approach for rotor mapping in cardiac tissue. *Chaos Interdiscipl. J. Nonlinear Sci.* 29:053101. doi: 10.1063/1.5086936
- Gurevich, D. R., Herndon, C., Uzelac, I., Fenton, F. H., and Grigoriev, R. O. (2017). “Level-set method for robust analysis of optical mapping recordings of fibrillation,” in *2017 Computing in Cardiology (CinC)* (Rennes), 1–4. doi: 10.22489/CinC.2017.197-427
- Hochreiter, S., and Schmidhuber, J. (1997). Long short-term memory. *Neural Comput.* 9, 1735–1780. doi: 10.1162/neco.1997.9.8.1735
- Huang, X., Xu, W., Liang, J., Takagaki, K., Gao, X., and young Wu, J. (2010). Spiral wave dynamics in neocortex. *Neuron* 68, 978–990. doi: 10.1016/j.neuron.2010.11.007
- Hwang, M., Song, J.-S., Lee, Y.-S., Li, C., Shim, E. B., and Pak, H.-N. (2016). Electrophysiological rotor ablation in *in-silico* modeling of atrial fibrillation: comparisons with dominant frequency, Shannon entropy, and phase singularity. *PLoS ONE* 11:e0149695. doi: 10.1371/journal.pone.0149695
- Ioffe, S., and Szegedy, C. (2015). “Batch normalization: Accelerating deep network training by reducing internal covariate shift,” in *Proceedings of the 32nd International Conference on Machine Learning*, eds F. Bach and D. Blei (Lille: PMLR), 448–456.
- Iyer, A. N., and Gray, R. A. (2001). An experimentalist’s approach to accurate localization of phase singularities during reentry. *Ann. Biomed. Eng.* 29, 47–59. doi: 10.1114/1.1335538
- King, B., Porta-Sanchez, A., Masse, S., Zamiri, N., Balasundaram, K., Kusha, M., et al. (2017). Effect of spatial resolution and filtering on mapping cardiac fibrillation. *Heart Rhythm* 14, 608–615. doi: 10.1016/j.hrthm.2017.01.023
- Kingma, D. P., and Ba, J. (2015). Adam: a method for stochastic optimization. *arXiv [Preprint]*. arXiv:1412.6980
- Krinsky, V. I., Efimov, I. R., and Jalife, J. (1992). Vortices with linear cores in excitable media. *Proc. R. Soc. Lond. Ser. A Math. Phys. Sci.* 437, 645–655. doi: 10.1098/rspa.1992.0084
- Kuklik, P., Zeemering, S., Maesen, B., Maessen, J., Crijns, H. J., Verheule, S., et al. (2015). Reconstruction of instantaneous phase of unipolar atrial contact electrogram using a concept of sinusoidal recombination and Hilbert transform. *IEEE Trans. Biomed. Eng.* 62, 296–302. doi: 10.1109/TBME.2014.2350029
- Kuklik, P., Zeemering, S., van Hunnik, A., Maesen, B., Pison, L., Lau, D. H., et al. (2017). Identification of rotors during human atrial fibrillation using contact mapping and phase singularity detection: technical considerations. *IEEE Trans. Biomed. Eng.* 64, 310–318. doi: 10.1109/TBME.2016.2554660
- Kuramoto, Y. (1984). *Chemical Oscillations, Waves, and Turbulence*. Berlin; Heidelberg: Springer. doi: 10.1007/978-3-642-69689-3
- Lee, Y.-S., Song, J.-S., Hwang, M., Lim, B., Joung, B., and Pak, H.-N. (2016). A new efficient method for detecting phase singularity in cardiac fibrillation. *PLoS ONE* 11:e0167567. doi: 10.1371/journal.pone.0167567
- Li, T.-C., Pan, D.-B., Zhou, K., Jiang, R., Jiang, C., Zheng, B., et al. (2018). Jacobian-determinant method of identifying phase singularity during reentry. *Phys. Rev. E* 98:062405. doi: 10.1103/PhysRevE.98.062405
- Li, X., Almeida, T. P., Dastagir, N., Guillem, M. S., Salinet, J., Chu, G. S., et al. (2020). Standardizing single-frame phase singularity identification algorithms and parameters in phase mapping during human atrial fibrillation. *Front. Physiol.* 11:869. doi: 10.3389/fphys.2020.00869
- Liu, J., Totz, J. F., Miller, P. W., Hastewell, A. D., Chao, Y.-C., Dunkel, J., et al. (2021). Topological braiding and virtual particles on the cell membrane. *Proc. Natl. Acad. Sci. U.S.A.* 118. doi: 10.1073/pnas.2104191118
- Liu, Y.-B., Peter, A., Lamp, S. T., Weiss, J. N., Chen, P.-S., and Lin, S.-F. (2003). Spatiotemporal correlation between phase singularities and wavebreaks during ventricular fibrillation. *J. Cardiovasc. Electrophysiol.* 14, 1103–1109. doi: 10.1046/j.1540-8167.2003.03218.x
- Marcotte, C. D., and Grigoriev, R. O. (2017). Dynamical mechanism of atrial fibrillation: a topological approach. *Chaos Interdiscipl. J. Nonlinear Sci.* 27:093936. doi: 10.1063/1.5003259
- Martinez-Mateu, L., Romero, L., Ferrer-Albero, A., Sebastian, R., Rodriguez Matas, J. F., Jalife, J., et al. (2018). Factors affecting basket catheter detection of real and phantom rotors in the atria: a computational study. *PLoS Comput. Biol.* 14:e1006017. doi: 10.1371/journal.pcbi.1006017
- Mulimani, M. K., Alageshan, J. K., and Pandit, R. (2020). Deep-learning-assisted detection and termination of spiral and broken-spiral waves in mathematical models for cardiac tissue. *Phys. Rev. Res.* 2:023155. doi: 10.1103/PhysRevResearch.2.023155
- Munoz, V., Grzeda, K. R., Desplantez, T., Pandit, S. V., Mironov, S., Taffet, S. M., et al. (2007). Adenoviral expression of  $I_{Ks}$  contributes to wavebreak and fibrillatory conduction in neonatal rat ventricular cardiomyocyte monolayers. *Circ. Res.* 101, 475–483. doi: 10.1161/CIRCRESAHA.107.149617
- Nair, V., and Hinton, G. E. (2010). “Rectified linear units improve restricted Boltzmann machines,” in *ICML10* (Madison, WI: Omni Press), 807–814.

- Nash, M. P., Mourad, A., Clayton, R. H., Sutton, P. M., Bradley, C. P., Hayward, M., et al. (2006). Evidence for multiple mechanisms in human ventricular fibrillation. *Circulation* 114, 536–542. doi: 10.1161/CIRCULATIONAHA.105.602870
- Nattel, S., Xiong, F., and Aguilar, M. (2017). Demystifying rotors and their place in clinical translation of atrial fibrillation mechanisms. *Nat. Rev. Cardiol.* 14, 509–520. doi: 10.1038/nrcardio.2017.37
- Podziemski, P., Zeemering, S., Kuklik, P., van Hunnik, A., Maesen, B., Maessen, J., et al. (2018). Rotors detected by phase analysis of filtered, epicardial atrial fibrillation electrograms colocalize with regions of conduction block. *Circ. Arrhythmia Electrophysiol.* 11:e005858. doi: 10.1161/CIRCEP.117.005858
- Ribera, J., Guera, D., Chen, Y., and Delp, E. J. (2019). “Locating objects without bounding boxes,” in *2019 IEEE/CVF Conference on Computer Vision and Pattern Recognition (CVPR)* (Long Beach, CA). doi: 10.1109/cvpr.2019.00664
- Rodrigo, M., Climent, A. M., Liberos, A., Fernandez-Aviles, F., Berenfeld, O., Aienza, F., et al. (2017). Technical considerations on phase mapping for identification of atrial reentrant activity in direct- and inverse-computed electrograms. *Circ. Arrhythmia Electrophysiol.* 10:e005008. doi: 10.1161/CIRCEP.117.005008
- Rogers, J. (2004). Combined phase singularity and wavefront analysis for optical maps of ventricular fibrillation. *IEEE Trans. Biomed. Eng.* 51, 56–65. doi: 10.1109/TBME.2003.820341
- Roney, C., Wit, A. L., and Peters, N. (2019). Challenges associated with interpreting mechanisms of AF. *Arrhythmia Electrophysiol. Rev.* 8, 273–284. doi: 10.15420/aer.2019.08
- Roney, C. H., Cantwell, C. D., Bayer, J. D., Qureshi, N. A., Lim, P. B., Tweedy, J. H., et al. (2017). Spatial resolution requirements for accurate identification of drivers of atrial fibrillation. *Circ. Arrhythmia Electrophysiol.* 10:e004899. doi: 10.1161/CIRCEP.116.004899
- Ronneberger, O., Fischer, P., and Brox, T. (2015). “U-Net: convolutional networks for biomedical image segmentation,” in *Lecture Notes in Computer Science*, eds N. Navab, J. Hornegger, W. M. Wells, and A. F. Frangi (Cham: Springer International Publishing), 234–241. doi: 10.1007/978-3-319-24574-4\_28
- Schotten, U., Lee, S., Zeemering, S., and Waldo, A. L. (2020). Paradigm shifts in electrophysiological mechanisms of atrial fibrillation. *Europace* 23(Suppl\_2), ii9–ii13. doi: 10.1093/europace/eaab384
- Shi, X., Chen, Z., Wang, H., Yeung, D., Wong, W., and Woo, W. (2015). “Convolutional LSTM network: a machine learning approach for precipitation nowcasting,” in *Annual Conference on Neural Information Processing Systems 2015*, eds C. Cortes, N. D. Lawrence, D. D. Lee, M. Sugiyama, and R. Garnett (Montreal, QC), 802–810.
- Tan, T., Liu, J., Miller, P., Tekant, M., Dunkel, J., and Fakhri, N. (2020). Topological turbulence in the membrane of a living cell. *Nat. Phys.* 16, 657–662. doi: 10.1038/s41567-020-0841-9
- Taniguchi, D., Ishihara, S., Oonuki, T., Honda-Kitahara, M., Kaneko, K., and Sawai, S. (2013). Phase geometries of two-dimensional excitable waves govern self-organized morphodynamics of amoeboid cells. *Proc. Natl. Acad. Sci. U.S.A.* 110, 5016–5021. doi: 10.1073/pnas.1218025110
- Tomii, N., Yamazaki, M., Arafune, T., Honjo, H., Shibata, N., and Sakuma, I. (2016). Detection algorithm of phase singularity using phase variance analysis for epicardial optical mapping data. *IEEE Trans. Biomed. Eng.* 63, 1795–1803. doi: 10.1109/TBME.2015.2502726
- Umapathy, K., Nair, K., Masse, S., Krishnan, S., Rogers, J., Nash, M. P., et al. (2010). Phase mapping of cardiac fibrillation. *Circ. Arrhythmia Electrophysiol.* 3, 105–114. doi: 10.1161/CIRCEP.110.853804
- Valderrabano, M., Chen, P.-S., and Lin, S.-F. (2003). Spatial distribution of phase singularities in ventricular fibrillation. *Circulation* 108, 354–359. doi: 10.1161/01.CIR.0000080322.67408.B4
- Van Nieuwenhuysse, E., Martinez-Mateu, L., Saiz, J., Panfilov, A. V., and Vandersickel, N. (2021). Directed graph mapping exceeds phase mapping in discriminating true and false rotors detected with a basket catheter in a complex *in-silico* excitation pattern. *Comput. Biol. Med.* 133:104381. doi: 10.1016/j.compbiomed.2021.104381
- Vandersickel, N., Van Nieuwenhuysse, E., Van Cleemput, N., Goedgebeur, J., El Haddad, M., De Neve, J., et al. (2019). Directed networks as a novel way to describe and analyze cardiac excitation: directed graph mapping. *Front. Physiol.* 10:1138. doi: 10.3389/fphys.2019.01138
- Vincent, P., Laroche, H., Bengio, Y., and Manzagol, P.-A. (2008). *Extracting and Composing Robust Features with Denoising Autoencoders*. Helsinki: Association for Computing Machinery. doi: 10.1145/1390156.1390294
- Winfrey, A. T. (1989). Electrical instability in cardiac muscle: phase singularities and rotors. *J. Theoret. Biol.* 138, 353–405. doi: 10.1016/S0022-5193(89)80200-0
- Witkowski, F. X., Leon, L. J., Penkoske, P. A., Giles, W. R., Spano, M. L., Ditto, W. L., et al. (1998). Spatiotemporal evolution of ventricular fibrillation. *Nature* 392, 78–82. doi: 10.1038/32170
- Yamazaki, M., Mironov, S., Taravant, C., Brec, J., Vaquero, L. M., Bandaru, K., et al. (2012). Heterogeneous atrial wall thickness and stretch promote scroll waves anchoring during atrial fibrillation. *Cardiovasc. Res.* 94, 48–57. doi: 10.1093/cvr/cvr357
- You, M. J., Langfield, P., Campanari, L., Dobbs, M., Shrier, A., and Glass, L. (2017). Demonstration of cardiac rotor and source mapping techniques in embryonic chick monolayers. *Chaos Interdiscipl. J. Nonlinear Sci.* 27:093938. doi: 10.1063/1.5001459
- Zaitsev, A. V., Guha, P. K., Sarmast, F., Kolli, A., Berenfeld, O., Pertsov, A. M., et al. (2003). Wavebreak formation during ventricular fibrillation in the isolated, regionally ischemic pig heart. *Circ. Res.* 92, 546–553. doi: 10.1161/01.RES.0000061917.23107.F7
- Zaritski, R., Mironov, S. F., and Pertsov, A. M. (2004). Intermittent self-organization of scroll wave turbulence in three-dimensional excitable media. *Phys. Rev. Lett.* 23:168302. doi: 10.1103/PhysRevLett.92.168302
- Zou, R., Kneller, J., Leon, L. J., and Nattel, S. (2002). Development of a computer algorithm for the detection of phase singularities and initial application to analyze simulations of atrial fibrillation. *Chaos Interdiscipl. J. Nonlinear Sci.* 12, 764–778. doi: 10.1063/1.1497505

**Conflict of Interest:** The authors declare that the research was conducted in the absence of any commercial or financial relationships that could be construed as a potential conflict of interest.

**Publisher’s Note:** All claims expressed in this article are solely those of the authors and do not necessarily represent those of their affiliated organizations, or those of the publisher, the editors and the reviewers. Any product that may be evaluated in this article, or claim that may be made by its manufacturer, is not guaranteed or endorsed by the publisher.

Copyright © 2021 Lebert, Ravi, Fenton and Christoph. This is an open-access article distributed under the terms of the Creative Commons Attribution License (CC BY). The use, distribution or reproduction in other forums is permitted, provided the original author(s) and the copyright owner(s) are credited and that the original publication in this journal is cited, in accordance with accepted academic practice. No use, distribution or reproduction is permitted which does not comply with these terms.